Numerical and Analytic Theory of Gray Molasses Cooling

by

Arnon Robert Goldberg

A thesis submitted to the Faculty of the

University of Colorado in partial fulfillment

of the requirements for the degree of

Bachelor of Arts

Department of Physics

2022

Defense Date: April 1, 2022

Committee Members:

Murray Holland, Physics, Chair

Jem Corcoran, Applied Mathematics

Daniel Dessau, Physics

Goldberg, Arnon Robert (B.S., Engineering Physics)

Numerical and Analytic Theory of Gray Molasses Cooling

Thesis directed by Prof. Murray Holland, Physics

In the simulation and analysis of atom-laser interactions that involve a large Hilbert space, and in particular laser cooling processes for systems containing multiple energy levels, the majority of papers have relied on semiclassical approximations and analytic solutions to simplified models. However, recent developments in computational speed and power have allowed us to study fully quantum numeric results in more complex systems than previously possible. This maintains the ability to study the effects of superpositions and atomic coherences that become increasingly important at low temperatures. We present a fully quantum Monte Carlo wave function simulation method that allows us to model the wave function in three dimensions, and in limited systems with arbitrary non-degenerate energy manifolds. We employ this technique to examine multiple atomic systems in including Doppler, polarization gradient, and gray molasses cooling. We also develop analytic descriptions for the resonance effects of dark states and velocity selective coherent population trapping using an Adiabatic elimination technique that employs an effective operator formalism. Our work is motivated by the desire to understand laser cooling in complex systems such as molecules that possess many internal degrees of freedom.

Dedication

To my family.

Acknowledgements

I am incredibly grateful for the opportunity I received as an undergraduate at University of Colorado, Boulder. I arrived at CU without any plan except that I wanted to study physics. I chanced upon a poster for a presentation given by Jarrod Reilly through the CU Prime organization in Duane. That was my first exposure to laser physics, and ignited a deep passion for this field. It wasn't long before I joined Dr. Murray Holland's theory group. Murray spent many hours mentoring me as I learned the fundamentals of atomic, molecular and optical physics. During my first few months with the group, I also received a great deal of mentorship from John Bartolotta, a fifth year graduate student in the group. He introduced me to Gray Molasses Cooling, and led me through the early stages of the project. As I progressed, I also worked closely with Jarrod. His advice and intuition for laser cooling was invaluable for my progression through this project. Finally, I would like to thank Simon Jaeger, John Wilson, Gage Harmon, and Lilian Chih for all of conversations and advice I received along the way.

Contents

Chapter

Figures

Figure

Chapter 1

Introduction and Background

Atomic, molecular, and optical physicists have been studying ultra-cold clouds of atoms and molecules for over half a century. Since first theoretically predicting [9] and demonstrating Doppler cooling in an experimental setup [26], leading physicists in the field have been striving to create colder, longer lived, and larger samples of ultra-cold particles with more complex internal structures. Not long after the first Doppler cooling schemes were developed, experimental groups began observing sub-Doppler temperatures in their labs [14]. Sub-Doppler cooling was quickly explained with theories such as coherent population trapping and polarization gradient cooling [4] [3].

Even as physicists explained new phenomena, experimentalists delved deeper into more complex systems, achieving colder temperatures. Recently, experimentalists have achieved some of the lowest temperatures of directly laser-cooled ensembles yet, employing a technique called Λ-enhanced gray molasses cooling (GMC). This technique couples traditional polarization gradient cooling with velocity selective coherent population trapping (VSCPT), resulting in large friction forces and low scattering rates in low momentum states. This technique has been experimentally verified in potassium, rubidium, lithium, and yttrium monoxide (YO) [5][8] [24][22].

While current theory qualitatively describes the behavior of Λ-enhanced gray molasses cooling, we currently have no model to precisely predict temperatures. Additionally, certain characteristics common to atoms and molecules cooled under this laser scheme remain unexplained. In particular, as the Raman condition is varied near resonance, experimental groups observe dra-

matic increases in temperature. In this thesis, I will employ numerical simulations and analytical techniques to describe the behavior gray molasses cooling systems.

1.1 Monte Carlo Wave Functions

In this thesis, I use Monte Carlo wave-functions (MCWF) or the quantum jump method to numerically simulate laser cooling. I will also discuss theoretical explanations for the results observed in experiments that motivated this study, and the simulations that I conduct. The MCWF method is equivalent to the Lindblad form of the master equation when infinite trajectories are taken, and so our simulations must use a sufficient number of trajectories to produce reliable results. At its simplest, the MCWF tracks each of the internal and external degrees of freedom of an atom or molecule. MCWF employs an numeric integration scheme by operating an interaction Hamiltonian upon a tensor containing an atom's internal state population and momentum wave function.

I will begin with a brief description of MCWF, and from there expand the procedure to the more complex systems necessary for GMC. First presented in 1992 [17], MCWF works by separating the equations of motion into a Hermitian and non-Hermitian Hamiltonian. The prior represents the evolution of an atom or molecule with the laser field, and the latter represents the non-unitary evolution due to spontaneous emission.

For simplicity, I begin by calculating a Hamiltonian for a two level atom, evolving in one dimension, following the procedure outlined in [25], [23], and similarly employed in [20]. This Hamiltonian may be employed to study Doppler Cooling. The Hermitian portion of the calculation takes the form

$$\hat{H} = \frac{\hbar\omega_a}{2}\hat{\sigma}_z + \frac{\hat{p}^2}{2m} + \hat{H}_{\text{int}} \ , \tag{1.1}$$

where I have defined the atomic Pauli z-operator as $\hat{\sigma}_z = |e\rangle\langle e| - |g\rangle\langle g|$, and the momentum operator as $\hat{p} = p|p\rangle\langle p|$. The interaction Hamiltonian $\hat{H}_{\text{int}}$ after the dipole and rotating wave approximations can be written as

$$\hat{H}_{\text{int}} = \frac{\hbar\Omega}{2}\left(\hat{\sigma}_- e^{-i[k\hat{x}-\omega t]} + h.c.\right) + \frac{\hbar\Omega}{2}\left(\hat{\sigma}_- e^{i[k\hat{x}+\omega t]} + h.c.\right) \ . \tag{1.2}$$

In this calculation, I defined the raising (lowering) operator as $\hat{\sigma}_+ = |e\rangle\langle g|$, ($\hat{\sigma}_- = |g\rangle\langle e|$). I have defined the position operator $\hat{x}$ such that the momentum raising (lowering) operator is $e^{ik\hat{x}} = |p + \hbar k\rangle\langle p|$, ($e^{-ik\hat{x}} = |p - \hbar k\rangle\langle p|$). Finally we define the Rabi frequency Ω under the assumption that the left and right oriented lasers have the same frequency and intensity, such that

$$\Omega = -\frac{E_0}{\hbar}\langle g|\hat{\varepsilon}\cdot\hat{\boldsymbol{d}}|e\rangle. \tag{1.3}$$

In this equation, E_0 is the magnitude of the electric field, ε is the polarization of the field, and $\hat{\boldsymbol{d}}$ is the dipole operator. In order to numerically solve the Hamiltonian, it is necessary to move into the interaction picture, or a rotating frame of reference. The rotating frame allows us to disregard large frequencies in the calculation, and instead focus on the much smaller relative values. In other words, while the the atomic frequency may be on the order of gigahertz, we are only concerned with the difference (detuning) between the atomic and laser frequencies, which tends to be many orders of magnitude smaller. Moving into this frame allows for an elegant mathematical depiction of the Hamiltonian, and far more efficient numeric integration, due the smaller frequencies. By defining an interaction picture

$$\hat{H}' = \frac{\hbar\omega_l}{2}\hat{\sigma}_z + \frac{\hat{p_l}^2}{2m}\ , \tag{1.4}$$

where ω_l is the laser frequency, such that our new Hamiltonian is $\tilde{\hat{H}} = e^{\frac{i\hat{H}'t}{\hbar}}[\hat{H} - \hat{H}']e^{\frac{-i\hat{H}'t}{\hbar}}$, which is equivalent to

$$\tilde{\hat{H}} = \frac{\hbar\Delta}{2}\hat{\sigma}_z + \frac{\hbar\Omega}{2}\big(\hat{\sigma}_- e^{-i\omega_r t(2\beta+1)}|\beta\rangle\langle\beta+1| + h.c.\big) + \frac{\hbar\Omega}{2}\big(\hat{\sigma}_+ e^{i\omega_r t(2\beta-1)}|\beta\rangle\langle\beta-1| + h.c.\big)\ . \tag{1.5}$$

The first term corresponds to the effect of detuning between the laser and the atoms such that $\Delta = \omega_a - \omega_l$. The second (third) term corresponds to the left (right) laser, such that the recoil frequency $\omega_r = \frac{\hbar k^2}{2m}$, and the dimensionless momentum $\hat{\beta} = \frac{\hat{p}}{\hbar k}$. A rigorous derivation of this Hamiltonian is given in appendix A.

Now that we have derived the Hermitian Hamiltonian, we must add in spontaneous emission in order to have a complete picture of the atomic evolution. We generate spontaneous emission events according to the methods outlined in [10]. The norm of the wave function undergoes exponential decay according to the spontaneous emission rate Γ, and the excited state population, such

that the non-Hermitian Hamiltonian for the two level system corresponds to $\hat{H}_{nh} = \frac{-i\hbar\Gamma}{2}|e\rangle\langle e|$. We then apply the total Hamiltonian $\hat{H}_{tot} = \tilde{\hat{H}} + \hat{H}_{nh}$ to the momentum wave function, and evolve the system over sufficiently small time steps by employing fourth-order Runge-Kutta integration. The jump operator is simulated in the system by generating a uniform random variable. When the norm decays below this value, the excited state population is transferred into the ground, indicating that the excited state has emitted a photon. Another pair of random variables are then generated, and used to simulate the direction of the photon emission according to the dipole radiation pattern. The momentum grid is then shifted by $\hbar k$ away from the direction of emission, corresponding to the momentum kick the atom experiences from spontaneous emission.

1.2 Doppler Cooling in One-Dimension

The most fundamental form of laser cooling is Doppler cooling. This cooling mechanism works on simple atoms and molecules by applying a pair of counter-propagating lasers to the system. Each of these lasers drive absorption and stimulated emission along the direction of laser propagation. Each laser is red detuned from resonance, resulting in stronger interaction with the laser the atom is moving towards as it is blue-shifted near resonance. This effect is coupled with the fact that over infinite spontaneous emissions, the average change in momentum is zero. Thus, as the atom moves toward a laser, there is a higher probability that it absorbs a photon from the laser it is moving into than the one it is moving away from, reducing the magnitude of its momentum. The rate of absorption is also greater than the rate of stimulated emission, due to spontaneous emission, which has a net zero effect on momentum. By combining all of these effects, an average force on the atom can be derived, driving the atom toward zero momentum.

Although the force in Doppler cooling is driving the temperature toward zero momentum, the theoretical temperature limit is in fact much greater. This comes from the fact that the atom laser interaction, and the randomness of spontaneous emission results in momentum diffusion. Although the momentum distribution is centered at zero momentum, it has a nonzero variance, resulting in a temperature of $k_b T = \frac{\hbar\Gamma}{4}\frac{1+(2\Delta/\Gamma)^2}{(-2\Delta/\Gamma)}$. We find the temperature minimum when $\Delta = -\Gamma/2$, which

yield the Doppler cooling limit $k_b T = \frac{\hbar\Gamma}{2}$. In depth explanations for calculating temperature from the diffusion coefficients are given in [1, 4, 16, 25]. Similar techniques are employed in calculating temperature limits in the sub-Doppler cooling regime.

In our code, we evolve the dimensionless Hamiltonian such that $\omega_r = 1$. Thus, in order to find the dimensionless temperature, $T^{'} = T\frac{k_b}{\hbar}$, in one dimension, we begin with

$$\frac{1}{2}k_b T = \frac{1}{2}m_a\langle v^2\rangle \ , \tag{1.6}$$

where k_b is Boltzmann's constant and m_a is the atomic mass. We can then substitute in $v = \frac{n\hbar k}{m_a}$ and the recoil frequency, and rearrange to find

$$T^{'} = n^2\frac{\hbar k^2}{m_a} = 2n^2\omega_r \ . \tag{1.7}$$

Finally, we extract the n^2 value from a Gaussian fit of the momentum distribution. Because $\omega_r = 1$, the dimensionless temperature of a distribution calculated in our code corresponds to twice its variance. We demonstrate this in Fig. 1.1, where we evolve a single atomic trajectory, and histogram its momentum distribution once it has reached equilibrium. In this simulation we fixed $\Gamma = 100$, so we predict $T_d^{'} = 50$. Instead we find $T^{'} = 30.3$, which is slightly below the theoretical Doppler cooling limit, but remains on the same order of magnitude.

1.3 Polarization Gradient Cooling in a Lin $\perp$ Lin Configuration

After initial Doppler techniques were demonstrated experimentally, scientists began to observe temperatures well below the theoretical temperate limit. These sub-Doppler cooling effects were first explained by Dalibard and Tannoudji [4]. Polarization gradient cooling techniques rely on spatial variations in the polarization of the laser field. These techniques can generally be divided into two categories, Lin $\perp$ Lin and σ_+ - σ_-, both of which we will qualitatively demonstrate in this section and section 1.4.

Lin $\perp$ Lin cooling requires two counter propagating lasers, which are linearly polarized with respect to one another and the axis of propagation. The simplest configuration where this form

Figure 1.1: This plot shows the momentum distribution for a V type system, with $J_g = 0$ and $J_e = 1$, such that there is one ground state connected to two excited states with σ_+ - σ_- light. There are two counter-propagating circularly polarized beams with intensity $\Omega = 20$. In this system $\Gamma = 100$, and $\Delta = -50$. The histogram (blue) is the momentum distribution of eight trajectories averaged over a time $\frac{7000}{\Gamma}$. The Gaussian fit (red) yields the dimensionless temperature from twice its variance $T^{'} = 2\sigma^2 = 30.3$

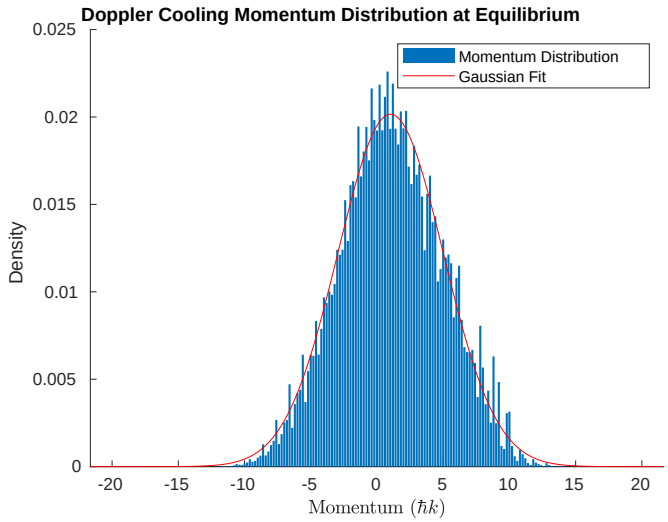

of cooling occurs is in $F_g = 1/2$ and $F_e = 3/2$, shown in Fig. 1.2, from [4]. With some clever rearrangements, the atom field interaction Hamiltonian for this system can be written as

$$\begin{aligned}\hat{H}_{af} = \frac{\hbar\Omega}{\sqrt{2}} \sin kz \left[|e_{3/2}\rangle\langle g_{1/2}| + \frac{1}{\sqrt{3}} |e_{1/2}\rangle\langle g_{-1/2}| \right] e^{-i\omega_l t} \\ + \frac{\hbar\Omega}{\sqrt{2}} \cos kz \left[|e_{-3/2}\rangle\langle -g_{1/2}| + \frac{1}{\sqrt{3}} |e_{-1/2}\rangle\langle g_{-1/2}| \right] e^{-i\omega_l t} + h.c.\end{aligned} \tag{1.8}$$

The polarization gradient effect manifests in the spatial dependence of the laser field in the sinusoidal terms, as shown in Fig. 1.3 from [4]. The varying field creates a large velocity-dependent force at low momentum. The atom is driven up the potential well, and spontaneously emits to the bottom of the well, resulting in a net decrease in energy. The cooling from this process is exceptionally strong, resulting in an equilibrium temperature of

$$k_b T \approx \frac{\hbar\Omega^2}{8|\delta|} \ . \tag{1.9}$$

However, due to the velocity sensitivity of this process, significant cooling only occurs when $kv \ll \Gamma$. This is because at greater velocities, the atom is no longer more likely to emit into a low energy state, as the spatial dependence of the field is averaged out. Because this cooling occurs only at very low velocities, it becomes quite difficult to simulate, as trajectories not trapped within just a few recoil frequency tend to diverge, and interact with the boundary of the momentum grid. In order to account for this effect, a very large momentum grid is required, allowing for the significant population loss that occurs in this configuration. Extracting the momentum would be done by creating a momentum histogram of all these trajectories, calculating the variance when it reaches equilibrium. A momentum grid of this scale takes a great deal of time to simulate. For this reason, we omit numerical analysis in this configuration.

1.4 Polarization Gradient Cooling in a σ_+ - σ_- Configuration

Another polarization gradient effect in laser cooling arises in systems comprised of two counter-propagating beams of circularly polarized light. The combination of the two circularly polarized beams results in a linear polarization, which rotates in space at an angle of $\theta = kz$, as

Figure 1.2: *Note.* This figure was created by J. Dalibard and C. Cohen-Tannoudji, *Laser cooling below the Doppler limit by polarization gradients: simple theoretical models* [4]. It depicts the degeneracy of both the excited and ground state manifolds, and the Clebsch-Gordon Coefficients connecting these manifolds.

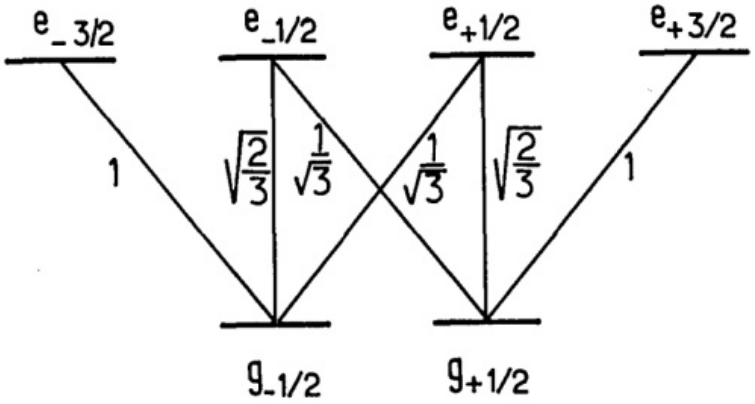

Figure 1.3: *Note.* This figure was created by J. Dalibard and C. Cohen-Tannoudji, *Laser cooling below the Doppler limit by polarization gradients: simple theoretical models* [4]. The figure (a) depicts the polarization gradient in σ_+ - σ_- light, where the helical shape is the field as experienced by the atom. The figure (b) depicts polarization gradient in the Lin $\perp$ Lin configuration. The parts (c) and (d) depict the spatially dependent shift in ground state energy for the σ_+ - σ_- and Lin $\perp$ Lin configuration respectively.

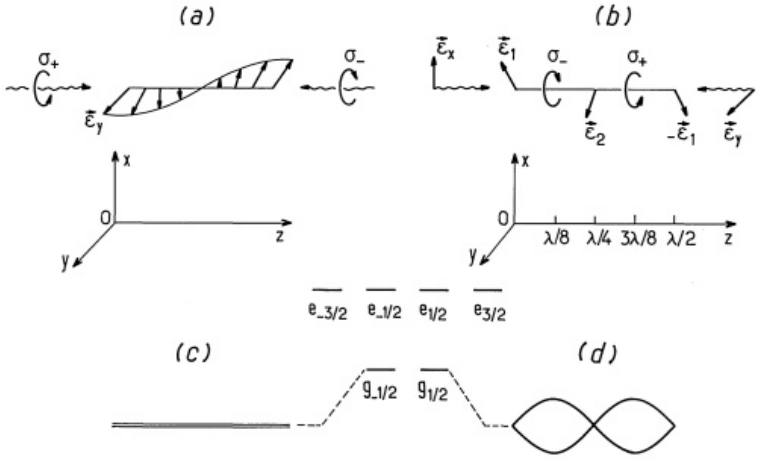

shown in Fig. 1.3. The varying polarization causes the atom or molecule to interact with each laser at different rates, resulting in a velocity-dependent force of greater magnitude than Doppler cooling at very low velocities. Unlike the Lin $\perp$ Lin configuration, this force is not restricted to the low velocity limit because it does not depend on emitting into the bottom of velocity induced potential wells. This means that simulating this cooling is significantly easier, as the higher velocity trajectories are still cooled. The cooling from this polarization gradient is calculated extensively in [4], resulting in a theoretical temperature limit of

$$k_b T = \frac{\hbar\Omega^2}{|\delta|}\left[\frac{29}{300} + \frac{245}{74}\frac{\Gamma^2/4}{\delta^2 + \Gamma^2/4}\right] . \tag{1.10}$$

This force arises in the $F_g = 1$ to $F_e = 2$ transition, as well as a fictional W-type transition, with three excited states, and two ground states. As we will show later in this thesis, both of these transitions occur in gray molasses configurations. Polarization gradients have been demonstrated experimentally in [12, 11, 6]. We demonstrate the occurrence of sub-Doppler polarization gradient cooling on a W-type transition in Fig. 1.4. In this simulation, we set $\Gamma = \Omega = 100$, and $\Delta = 4.5\Gamma$. Because the lasers are far detuned, we expect to see no Doppler cooling in this system. After evolution, we can extract three temperatures. The first corresponds to a Gaussian fit where $T^{'} = 66.1$. Note that this temperature actually increased from the Doppler limit. The other temperatures correspond to a double Gaussian fit where in Fig. 1.4, the tighter Gaussian corresponds to $T^{'} = 6.3$, and the wider Gaussian corresponds to $T^{'} = 102.91$. This indicates that in the parameter regime of the simulation, the high velocity force is much smaller than in Doppler cooling, but the low velocity force is much greater. If we choose parameters in which Doppler cooling occurs with $\Delta = -\frac{\Gamma}{2}$, we can achieve much lower temperatures, however it is less clear that these values derive from the polarization gradient, as traditional Doppler cooling may occur.

1.5 Sub-recoil cooling by Velocity Selective Coherent Population Trapping

Another essential ingredient to the ultra-cold temperatures observed in gray molasses configurations is velocity selective coherent population trapping (VSCPT) [3]. VSCPT occurs when a

Figure 1.4: This plot shows the momentum distribution for W type system, with two ground states, $m = \pm 1$, and three excited states, $m = 0, \pm 2$. The σ_+ - σ_- transitions between these states form a W shape. In the histogram, we have set $\Gamma = 100$, $\Delta = 450$, $\Omega = 100$. In the histogram, we have averaged the momentum distributions of 400 different trajectories between times $\frac{440}{\Gamma}$ and $\frac{660}{\Gamma}$. The two lines correspond to (red) a single Gaussian fit with $T^{'} = 66.1$, and a (green) double Gaussian fit with the narrower fit having $T^{'} = 6.3$, and the wider having $T^{'} = 102.91$.

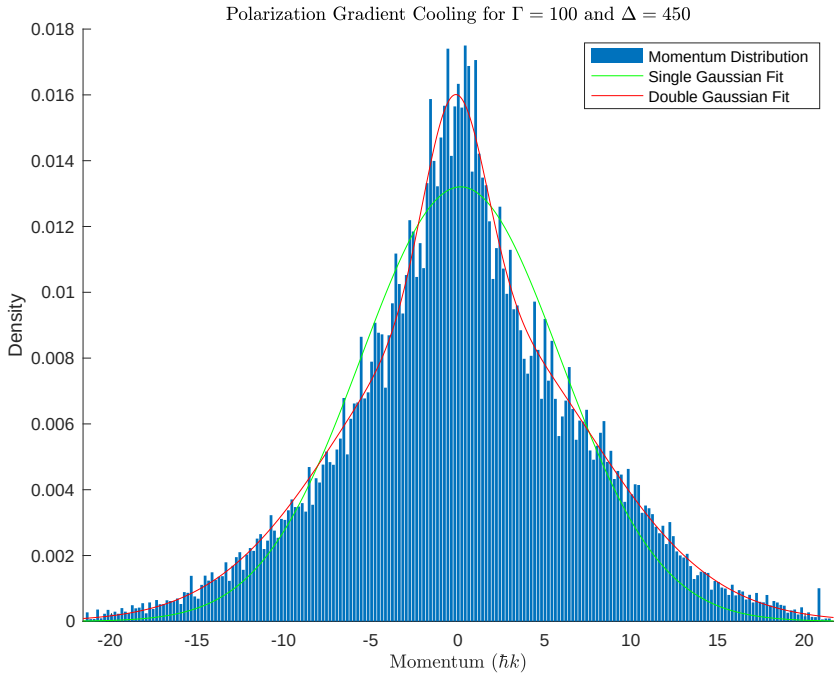

population of atoms or molecules ceases to interact with a laser field due to interference effects in the system. The most common and simplest system wherein this effect is observed is the $J_g = 1$ to $J_e = 1$ configuration interacting with σ_+ - σ_- light. This configuration results in the system being pumped into a Λ-system with one excited state and two ground states, illustrated in Fig. 1.5. The dark state occurs in this system when the Raman condition is met, $\Delta_1 = \Delta_2$, and when the population is in the state

$$|\psi_{nc}\rangle = \frac{1}{\sqrt{2}}(|g_1, -\hbar k\rangle - |g_2, \hbar k\rangle) \ . \tag{1.11}$$

This calculation has been extended into two and three dimensions, and demonstrated experimentally in [13, 18]. In essence, the dark state observed in the Λ-configuration derives from the extreme symmetry of the system. Each ground state is driving populations of equal magnitude and opposite amplitude into the excited state, resulting in a net zero evolution. Furthermore, there is no population in the excited state, so the system does not spontaneously emit. This sub-recoil cooling is demonstrated in our code in Fig. 1.6. Although this configuration results in a small portion of the population being cooled below the recoil limit, there is quite a bit of population loss, because there are no other cooling effects in the Λ-system. We will conduct deeper analysis of the VSCPT effects in later sections of this thesis by introducing phases between the lasers, altering the intensities, and perturbing the detuning from the Raman condition.

Figure 1.5: This figure shows the Λ configuration found in the $J_g = 1$ to $J_e = 1$ system. The arrows represent the transitions addressed by the σ_+ - σ_- lasers. The left laser interacts with only m = -1 to m = 0 transition, and the right laser interacts with only the m = 1 to m = 0 transition.

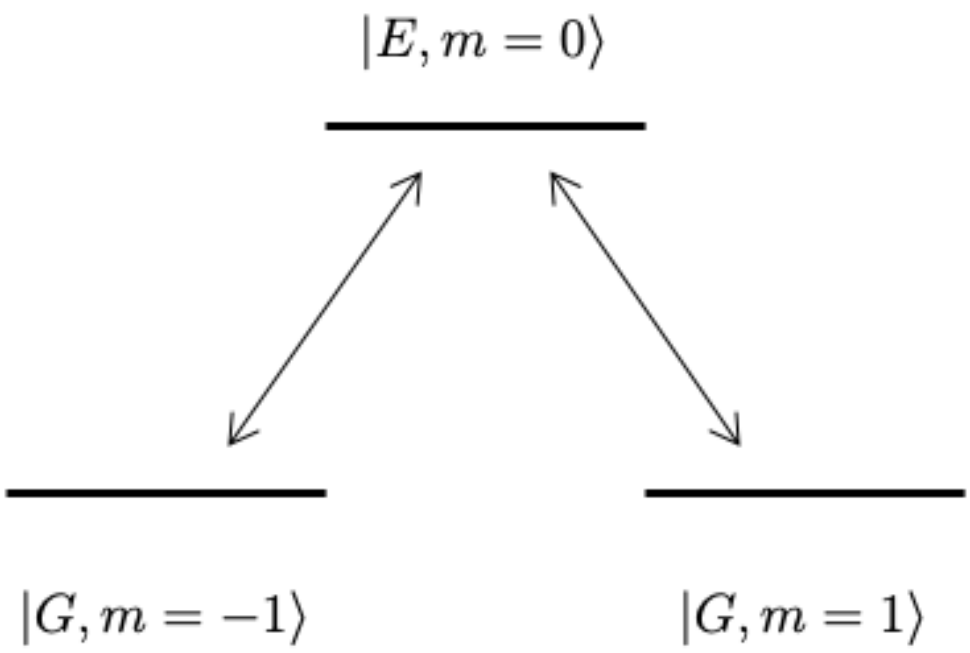

Figure 1.6: This plot shows the momentum distribution after sufficient spontaneous emissions to disperse the bright states, in the Λ system. Note that while the majority of the population diverges, about a quarter remains at $\pm\hbar k$, due to VSCPT. This small population is cooled to below the one recoil limit, while the remainder of the population remains unaddressed. This population distribution is averaged over 800 trajectories.

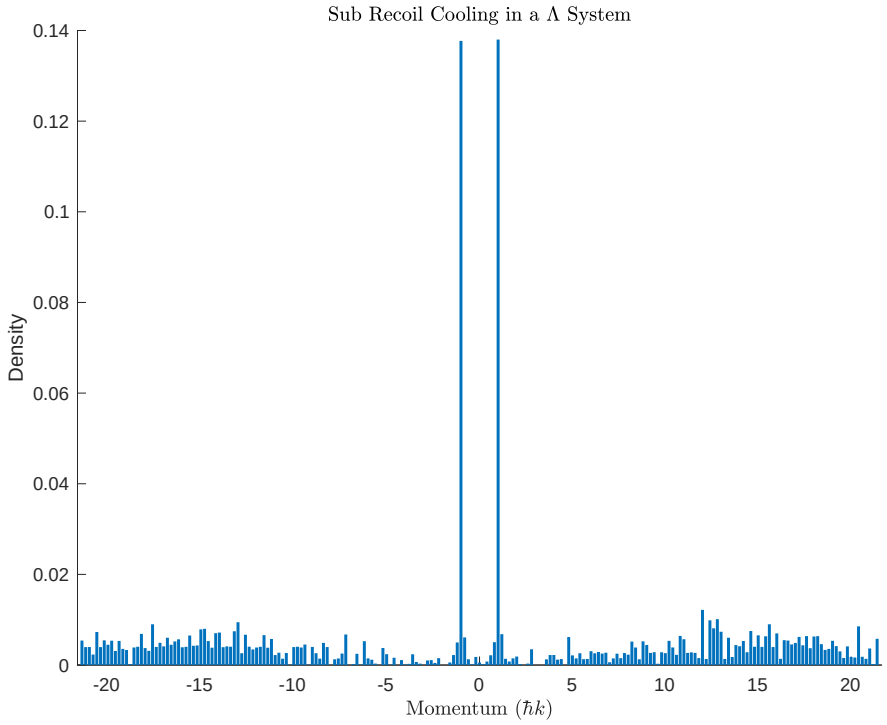

Chapter 2

Methods

In this chapter, we discuss the extension to the Monte Carlo wave function method that we employ in our code. The Monte Carlo extension and code serves as the backbone for the numerical analysis that we conduct throughout this thesis. We begin by calculating the Hamiltonian for our system. We then show a brief proof for time-reversal symmetry in the Hamiltonian, and demonstrate how this can be used to significantly simplify the code. We also introduce an effective operator formalism for elimination of the excited states developed by Reiter and Sørenson [21], and identify the characteristics of dark states in the Λ-system.

2.1 Extending Monte Carlo Wave Functions to Three-Dimensions and Multiple Energy Manifolds

We begin this chapter by solving the interaction Hamiltonian for three energy manifolds, two ground states, and one excited state, with arbitrary degeneracy. The two ground state manifolds are written as $|g_1\rangle$ and $|g_2\rangle$, and the excited manifold is $|e\rangle$. The interaction is driven by two pairs of counter-propagating lasers, with Rabi frequencies Ω_1 and Ω_2. Furthermore, we assume that the lasers address only their intended transitions, so laser one interacts only with $|g_1\rangle\langle e|$, and laser two

interacts only with $|g_2\rangle\langle e|$. We begin with a Hamiltonian of the form

$$\begin{aligned}\hat{H}_{\text{org}} = &\sum_{l=x,y,z} \frac{\hat{p}_l^2}{2m} - \hbar\omega_{a,1}|g_1\rangle\langle g_1| - \hbar\omega_{a,2}|g_2\rangle\langle g_2| \\ &+ \sum_{l=x,y,z} \frac{\hbar\Omega_{1,l}}{2}\left(\hat{\sigma}_1^- e^{-i[k\hat{x}_l-\omega_1 t]} + h.c.\right) + \frac{\hbar\Omega_{1,l}}{2}\left(\hat{\sigma}_1^- e^{i[k\hat{x}_l+\omega_1 t]} + h.c.\right) \\ &+ \sum_{l=x,y,z} \frac{\hbar\Omega_{2,l}}{2}\left(\hat{\sigma}_2^- e^{-i[k\hat{x}_l-\omega_2 t]} + h.c.\right) + \frac{\hbar\Omega_{2,l}}{2}\left(\hat{\sigma}_2^- e^{i[k\hat{x}_l+\omega_2 t]} + h.c.\right),\end{aligned} \tag{2.1}$$

where we define the Pauli operators $\hat{\sigma}_i^- = |e\rangle\langle g_i|$ and define all internal energies relative to the excited state. We also assume that $k \approx k_1 \approx k_2$, so that the momentum shift from the raising and lowering operators are equal, allowing us to evolve the wave function on a fixed grid in momentum space. We define $\Delta_i = \omega_i - \omega_{a,i}$ and then move into the rotating frame defined by

$$\hat{H}' = \sum_{l=x,y,z} \frac{\hat{p}_l^2}{2m} - \hbar\omega_1|g_1\rangle\langle g_1| - \hbar\omega_2|g_2\rangle\langle g_2| \ , \tag{2.2}$$

with the resulting interaction picture

$$\tilde{\hat{H}} = e^{\frac{i\hat{H}'t}{\hbar}}\left(\hat{H}_{\text{org}} - \hat{H}'\right)e^{\frac{-i\hat{H}'t}{\hbar}} \ , \tag{2.3}$$

where $\hat{H}_{org} - \hat{H}'$ can be rewritten as

$$\begin{aligned}\hat{H}_{\text{org}} - \hat{H}' = &\sum_{l=x,y,z} \hbar\Delta_1|g_1\rangle\langle g_1| + \hbar\Delta_2|g_2\rangle\langle g_2| \\ &+ \sum_{l=x,y,z} \frac{\hbar\Omega_{1,l}}{2}\left(\hat{\sigma}_1^- e^{-i[k\hat{x}_l-\omega_1 t]} + h.c.\right) + \frac{\hbar\Omega_{1,l}}{2}\left(\hat{\sigma}_1^- e^{i[k\hat{x}_l+\omega_1 t]} + h.c.\right) \\ &+ \sum_{l=x,y,z} \frac{\hbar\Omega_{2,l}}{2}\left(\hat{\sigma}_2^- e^{-i[k\hat{x}_l-\omega_2 t]} + h.c.\right) + \frac{\hbar\Omega_{2,l}}{2}\left(\hat{\sigma}_2^- e^{i[k\hat{x}_l+\omega_2 t]} + h.c.\right).\end{aligned} \tag{2.4}$$

Following a similar procedure to appendix A, we find the raising and lowering operators in the rotating frame

$$\dot{\tilde{\hat{\sigma}}}_i^+ = \frac{i}{\hbar}e^{\frac{i\hat{H}'t}{\hbar}}[\hat{H}', \sigma_i^+]e^{\frac{i\hat{H}'t}{\hbar}} = i\omega_i\tilde{\hat{\sigma}}_i^+ \ . \tag{2.5}$$

From here, it is straightforward to demonstrate that $\tilde{\hat{\sigma}}_i^+ = \hat{\sigma}_i^+ e^{i\omega_i t}$ and by the same process the

lowering operator is $\tilde{\hat{\sigma}}_i^- = \hat{\sigma}_i^- e^{-i\omega_i t}$. Substituting these values into the Hamiltonian gives us

$$\begin{aligned}\tilde{\hat{H}} = &\sum_{l=x,y,z} \hbar\Delta_1|g_1\rangle\langle g_1| + \hbar\Delta_2|g_2\rangle\langle g_2| \\ &+ \sum_{l=x,y,z} \frac{\hbar\Omega_{1,l}}{2}\left(\hat{\sigma}_1^- e^{-ik\tilde{\hat{x}}_l} + h.c.\right) + \frac{\hbar\Omega_{1,l}}{2}\left(\hat{\sigma}_1^- e^{ik\tilde{\hat{x}}_l} + h.c.\right) \\ &+ \sum_{l=x,y,z} \frac{\hbar\Omega_{2,l}}{2}\left(\hat{\sigma}_2^- e^{-ik\tilde{\hat{x}}} + h.c.\right) + \frac{\hbar\Omega_{2,l}}{2}\left(\hat{\sigma}_2^- e^{ik\tilde{\hat{x}}_l} + h.c.\right).\end{aligned} \tag{2.6}$$

Applying the Baker-Campbell formula in a similar fashion as in appendix A, substituting in the recoil frequency, and substituting $\hat{\beta} = \frac{\hat{p}}{\hbar k}$, we find a final Hamiltonian for the three manifold system

$$\begin{aligned}\tilde{\hat{H}} = &\sum_{l=x,y,z} \hbar\Delta_1|g_1\rangle\langle g_1| + \hbar\Delta_2|g_2\rangle\langle g_2| \\ &+ \sum_{l=x,y,z} \frac{\hbar\Omega_{1,l}}{2}\left(\hat{\sigma}_1^- e^{-i\omega_r t(2\beta+1)}|\beta\rangle\langle\beta+1| + h.c.\right) + \frac{\hbar\Omega_{1,l}}{2}\left(\hat{\sigma}_1^- e^{i\omega_r t(2\beta-1)}|\beta\rangle\langle\beta-1| + h.c.\right) \\ &+ \sum_{l=x,y,z} \frac{\hbar\Omega_{2,l}}{2}\left(\hat{\sigma}_2^- e^{-i\omega_r t(2\beta+1)}|\beta\rangle\langle\beta+1| + h.c.\right) + \frac{\hbar\Omega_{2,l}}{2}\left(\hat{\sigma}_2^- e^{i\omega_r t(2\beta-1)}|\beta\rangle\langle\beta-1| + h.c.\right).\end{aligned} \tag{2.7}$$

Simply including the degenerate levels of each manifold and considering the dipole operator element of the field yields the Hamiltonian for the Hermitian portion of the atom-laser interaction. The non-Hermitian portion of Hamiltonian derives directly from the spontaneous emission rates of each of the ground states that a given excited state may decay into via single-photon emission.

2.1.1 Time-Reversal Symmetry in our code

Because the atom-field interaction Hamiltonian must be Hermitian by definition, this means that each transition in the Hamiltonian must be time reversible. This means that the $|g,\beta\rangle\langle e,\beta+1|$ term is the Hermitian conjugate of the $|e,\beta+1\rangle\langle g,\beta|$ term. In our Hamiltonian, these transitions take the form $e^{-i\omega_r t(2\beta+1)}|\beta\rangle\langle\beta+1|$ and $e^{i\omega_r t(2\beta-1)}|\beta\rangle\langle\beta-1|$. It is easy to see that these terms are Hermitian conjugates from

$$\left(e^{-i\omega_r t(2\beta+1)}|\beta\rangle\langle\beta+1|\right)^\dagger = e^{i\omega_r t(2\beta+1)}|\beta+1\rangle\langle\beta|\ . \tag{2.8}$$

By noting that $|\beta+1\rangle\langle\beta| = |\beta\rangle\langle\beta-1|$, if we make the proper adjustment in the exponential term, Eq. (2.8) can be rearranged to read

$$\left(e^{-i\omega_r t(2\beta+1)}|\beta\rangle\langle\beta+1|\right)^\dagger = e^{i\omega_r t(2\beta-1)}|\beta\rangle\langle\beta-1| \ . \tag{2.9}$$

While we could hard code this symmetry in our Monte Carlo code, it is beneficial to simplify the form of the Hamiltonian, making the field terms more manageable and easily extendable. We begin by noting that each atomic trajectory is evolved on a momentum grid in a given dimension, which takes the form

$$p = \langle k-n, k-n+1, ..., k, ..., k+n-1, k+n\rangle \ , \tag{2.10}$$

where k is the center of the momentum grid, and n is an integer value denoting the width of the grid. The momentum raising and lowering operators move the trajectory along this grid, such that the β values must correspond to points on the grid. We can now divide vector Eq. (2.10) into two vectors of equal length $2n$:

$$\begin{aligned} N &= \langle -n, -n+1, ..., 0, ..., n-1, n\rangle \ , \\ K &= \langle k, k, ..., k, ..., k, k.\rangle \ . \end{aligned} \tag{2.11}$$

Thus, $p = N + K$. From here, we can define a momentum shift vector S, such that S is the $2n$ elements of $2p+1$. In other words we define S as the vector excluding the final element of the vector $2p+1$. Expanding S, we find

$$S = 2K + 2N + 1 \ . \tag{2.12}$$

We further define P_1 and P_2 as the first and last $2n$ elements of P, excluding the last and first element, respectively, giving

$$S = P_1 + P_2 \ . \tag{2.13}$$

The vector elements of the vector S can then be substituted into the exponential term in Eq. (2.8), because $\beta = 2(n+k)$. We need only multiply this vector by -1, to conjugate the complex exponential and move from the momentum raising to the lowering operator. This allows us to write

the field terms of the Hamiltonian in the code as Eq. (2.1), where this calculates the z-component of the evolution along the momentum grid. The momPhase function corresponds to the vector S, and fieldZ calculates a single laser operating on the state $|\psi\rangle$. This format allows us to account for arbitrarily many internal states, transitions, and lasers.

2.2 Adiabatic Elimination of the Excited States

In this section, we derive the Hamiltonians for VSCPT and lithium using an effective operator formalism for open quantum systems developed in [21]. This method allows us to calculate effective transitions between the ground states through the adiabatic elimination of the excited state manifold. This formalism is ideal for the study of dark states because the excited state population in these states is zero, and there is no spontaneous emission out of these states. For systems with multiple non-degenerate energy manifolds, we solve the effective Hamiltonian defined by

$$\hat{H}_{eff} = -\frac{1}{2}\big[\hat{V}_- \sum_{l=0}^{1} (\hat{H}_{nh}^{(l)})^{-1} \hat{V}_+^{(l)} + H.c.\big] + \hat{H}_g \ . \tag{2.14}$$

In this Hamiltonian, $\hat{H}_g$ is diagonalizable and can be written $\hat{H}_g = \sum_l E_l |F = l, \beta\rangle\langle F = l, \beta|$, where E_l corresponds to the energy difference between the ground and the excited manifolds. The internal raising (lowering) portion of the Hamiltonian are written V_+ (V_-). The non-Hermitian Hamiltonian is addressed on the excited state such that $\hat{H}_{nh} = \hbar \sum_l (\Delta_l - \frac{i\gamma}{2}) |e, \beta\rangle\langle e, \beta| = \hbar\tilde{\Delta}_l |e, \beta\rangle\langle e, \beta|$.

2.2.1 Three-Level System

We begin by addressing a simple three-level system, defined by two ground states $|g_1\rangle$ and $|g_2\rangle$ connected to an excited state $|e\rangle$ by σ_+ and σ_- light, respectively. This transition is the simplest system wherein VSCPT occurs. We move into the same frame that we use for multiple energy manifolds in Monte Carlo wave functions, where $\hat{H}_g = -\hbar\Delta_0 |g_0\rangle\langle g_0| - \hbar\Delta_1 |g_1\rangle\langle g_1|$. We define $\hat{V}_+$ and $\hat{V}_-$, noting that we have disregarded the Clebsch Gordon coefficients in this example, giving

Figure 2.1: Code

```
VectorXcd momPhase(const VectorXd& mom, const double t)
{
    VectorXd momHalf = mom.head(mom.size() - 1)
      + mom.tail(mom.size() - 1);
    return (I * momHalf * t).array().exp();
}
AtomState fieldZ(const VectorXd& mom, const AtomState &psi,
  const double t, Arrow arrow, const Laser& laser)
{
    AtomState psip(psi);
    setZero(psip);
    int n = mom.size();
    VectorXcd amplitude = momPhase(mom, t);
    Vector3cd pol = laser.pol;
    amplitude *= exp(I*laser.phase*t)*arrow.weight
      * transitionVec[arrow.label].dot(pol);
    if(abs(transitionVec[arrow.label].dot(pol)) > pow(10.,-3.))
    {
    for (int i = 0; i < psi[arrow.from].size(); i++)
    {
        for (int j = 0; j < psi[arrow.from][0].size(); j++)
        {
            psip[arrow.from][i][j].head(n-1) =
              amplitude.conjugate().cwiseProduct(
              psi[arrow.to][i][j].tail(n-1));
            psip[arrow.from][i][j][n-1] = ZERO;
            psip[arrow.to][i][j].tail(n-1) =
              amplitude.cwiseProduct(
              psi[arrow.from][i][j].head(n-1));
            psip[arrow.to][i][j][0] = ZERO;
            psip[arrow.to] *= -I * 0.5 * laser.intensity;
            psip[arrow.from] *= -I * 0.5 * laser.intensity;
        }
    }
    }
return psip;
}
```

$$\hat{V}_+ = \frac{\Omega_0}{2} e^{it(2\beta+1)} |e, \beta+1\rangle\langle\beta, 0| + e^{-it(2\beta+1)} |e, \beta-1\rangle\langle\beta, 1|$$
$$\hat{V}_- = \frac{\Omega_0}{2} e^{-it(2\beta+1)} |0, \beta\rangle\langle\beta+1, e| \frac{\Omega_1}{2} e^{it(2\beta-1)} |1, \beta\rangle\langle\beta-1, e| \ . \tag{2.15}$$

Finally, we define the non-Hermitian terms as $\hat{H}_{nh}^{(0)} = \hbar(\Delta_0 - \frac{i\gamma}{2})|e\rangle\langle e| = \hbar\tilde{\Delta}_0|e\rangle\langle e|$ and $\hat{H}_{nh}^{(1)} = \hbar\tilde{\Delta}_1|e\rangle\langle e|$. Combining these terms, we begin solving Eq. (2.14) by writing

$$\hat{V}_- \sum_{l=0}^{1} (\hat{H}_{nh}^{(l)})^{-1} \hat{V}_+^{(l)} = \hbar\big[\frac{\Omega_0}{2} e^{-it(2\beta+1)} |0, \beta\rangle\langle\beta+1, e| + \frac{\Omega_1}{2} e^{it(2\beta-1)} |1, \beta\rangle\langle\beta-1, e|\big]$$
$$\times\big[\frac{\Omega_0}{2\tilde{\Delta}_0} e^{it(2\beta+1)} |e, \beta+1\rangle\langle\beta, 0| + \frac{\Omega_1}{2\tilde{\Delta}_1} e^{-it(2\beta-1)} |e, \beta-1\rangle\langle\beta, 1|\big] \ . \tag{2.16}$$

Rearranging gives us

$$\hat{V}_- \sum_{l=0}^{1} (\hat{H}_{nh}^{(l)})^{-1} \hat{V}_+^{(l)} = \frac{\hbar\Omega_0^2}{4\tilde{\Delta}_0} |0, \beta\rangle\langle\beta, 0| + \frac{\hbar\Omega_1^2}{4\tilde{\Delta}_1} |1, \beta\rangle\langle\beta, 1| + \frac{\hbar\Omega_0\Omega_1}{4\tilde{\Delta}_0} |1, \beta+1\rangle\langle\beta-1, 0| e^{it(2\beta-1)} e^{it(2\beta+1)}$$
$$+ \frac{\hbar\Omega_0\Omega_1}{4\tilde{\Delta}_1} |0, \beta-1\rangle\langle\beta+1, 1| e^{-it(2\beta-1)} e^{-it(2\beta+1)} \ . \tag{2.17}$$

Finally, we can find the effective Hamiltonian by adding the Hermitian conjugate and ground state Hamiltonian

$$\hat{H}_{eff} = \hat{H}_g - \frac{\hbar\Delta_0\Omega_0^2}{4\Delta_0^2 + \gamma^2} |0, \beta\rangle\langle\beta, 0| - \frac{\hbar\Delta_1\Omega_1^2}{4\Delta_1^2 + \gamma^2} |1, \beta\rangle\langle\beta, 1|$$
$$- e^{it4\beta} \frac{\hbar\Omega_0\Omega_1(\Delta_0 + \Delta_1)}{8\tilde{\Delta}_0\tilde{\Delta}_1^\dagger} |1, \beta+1\rangle\langle\beta-1, 0| - e^{-it4\beta} \frac{\hbar\Omega_0\Omega_1(\Delta_0 + \Delta_1)}{8\tilde{\Delta}_0^\dagger\tilde{\Delta}_1} |0, \beta-1\rangle\langle\beta+1, 1|. \tag{2.18}$$

This provides an accurate approximation of the three level system. In order to study the dark states of this system, we simplify this equation by setting $\gamma = 0$, because there is no dissipation by spontaneous emission in the dark states. Furthermore, we let $\Delta_0 = \Delta_1 = \Delta$ to ensure that the Raman condition is met. Applying these simplifications to the system gives

$$\hat{H}_{eff} = \hat{H}_g - \frac{\hbar\Omega_0^2}{4\Delta} |0, \beta\rangle\langle\beta, 0| - \frac{\hbar\Omega_1^2}{4\Delta} |1, \beta\rangle\langle\beta, 1|$$
$$- \frac{\hbar\Omega_0\Omega_1}{4\Delta} |1, \beta+1\rangle\langle\beta-1, 0| - \frac{\hbar\Omega_0\Omega_1}{4\Delta} |0, \beta-1\rangle\langle\beta+1, 1|. \tag{2.19}$$

We now identify the dark state by searching for the kernel of the effective Hamiltonian. In other words, we want to find the non-evolving state, $|\psi\rangle_{dark} = a|\beta-1, 0\rangle + b|\beta+1, 1\rangle$, where a and

b correspond to the population in each of the ground states that remain constant as the system evolves. This occurs when $\beta = 0$ and the following system of equations is satisfied:

$$\begin{aligned} \frac{\Omega_0^2}{4\Delta} a &= -\frac{\Omega_0 \Omega_1}{4\Delta} b, \\ \frac{\Omega_1^2}{4\Delta} b &= -\frac{\Omega_0 \Omega_1}{4\Delta} a. \end{aligned} \tag{2.20}$$

These equations are solved to find

$$\begin{aligned} |a| &= \frac{\Omega_1}{\sqrt{\Omega_0^2 + \Omega_1^1}}, \\ |b| &= \frac{\Omega_0}{\sqrt{\Omega_0^2 + \Omega_1^1}}. \end{aligned} \tag{2.21}$$

where a is rotated 180 degrees around the complex unit circle from b. When $\Omega_1 = \Omega_2$, this solution agrees with Eq. (1.11). Thus, the dark state occurs around zero momentum, with the population in each state corresponding to the lasers Rabi frequencies. We have already shown this dark state and population transfer in Fig. 1.6. If we solve this same system with $\Omega_1 = \Omega_2$, but do not set $\beta = 0$, we find

$$\begin{aligned} a &= -e^{-4it\beta} b \ , \\ b &= -e^{4it\beta} a \ . \end{aligned} \tag{2.22}$$

This system is clearly not dark, as there is a time-dependent population transfer between the ground states, except for when $\beta = 0$ such that the system is on resonance.

2.2.2 Phases Between the Lasers in the Three-Level system

In the previous section we demonstrated VSCPT in the three-level system, and found that the ground states exchange population at a rate of $4\beta t$. In this section, we demonstrate that this phase can be eliminated, and dark states at varying momentum may be achieved, by introducing a term of the form $e^{i\delta t}$ onto one of the lasers. This term corresponds to a relative detuning between the lasers, which cannot be rotated out. We can extract this term by selecting a rotating frame of reference such that $\Delta_1 = \Delta_2$, but where one of these lasers is tuned slightly above or below this

resonance. Our interaction Hamiltonian then assumes the form

$$\begin{aligned}\hat{V} = \frac{\Omega_0}{2}\big(e^{-it(2\beta+1)}e^{i\delta t}|0,\beta\rangle\langle\beta+1,e| + e^{it(2\beta+1)}e^{-i\delta t}|e,\beta+1\rangle\langle\beta,0|\big) \\ +\frac{\Omega_1}{2}\big(e^{it(2\beta-1)}|1,\beta\rangle\langle\beta-1,e| + (e^{-it(2\beta+1)}|e,\beta-1\rangle\langle\beta,1|\big).\end{aligned} \tag{2.23}$$

The procedure for adiabatic elimination of the excited states remains unchanged, with the exception of the non-Hermitian term, which is modified to read $\hat{H}^{(0)}_{nh} = \hbar(\Delta_0 - \delta - \frac{i\gamma}{2})|e\rangle\langle e|$. By assuming that $\Delta_0 = \Delta_1 \gg \delta$, the non-Hermitian Hamiltonian remains approximately unchanged as $\hat{H}^{(0)}_{nh} = \hbar(\Delta_0 - \delta - \frac{i\gamma}{2})|e\rangle\langle e| \approx \hbar(\Delta_0 - \frac{i\gamma}{2})|e\rangle\langle e|$. Letting $\Omega_1 = \Omega_2$, Eq. (2.22) becomes.

$$\begin{aligned}a &= -e^{i\delta t}e^{-4it\beta}b, \\ b &= -e^{-i\delta t}e^{4it\beta}a.\end{aligned} \tag{2.24}$$

It is clear that this state is dark when $\delta = -4\beta$. Therefore, we can select the velocity at which dark states occur by introducing this detuning term between the lasers as shown in Fig. 2.2. This system is incredibly simple compared to YO and lithium 7, where we are concerned with 11 and 13 states, respectively. However, the necessity to introduce a detuning of similar form to Eq. (2.23) will become apparent in the subsequent sections, and the velocity selection this detuning allows will inform our solutions to the more complex systems.

Figure 2.2: In this plot each color corresponds to a different δ value on the right laser in the Λ-system.

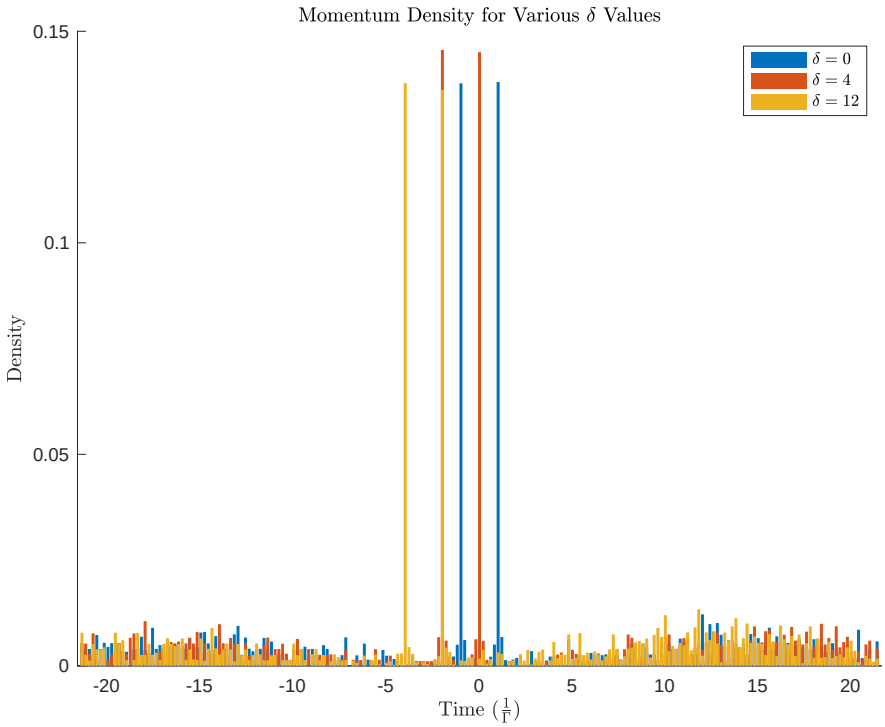

Chapter 3

Analysis and Results

In this chapter we apply the code to systems roughly equivalent to lithium-7 [8], where gray molasses cooling has been experimentally demonstrated, and compare our theoretical predictions from Monte Carlo wave functions to experimental observations. We analyze these results by employing an effective operator formalism for elimination of the excited states developed by Reiter and Sørensen [21], and identify the characteristics of dark states in the lithium system. Finally, we introduce Fano [15, 7] profiles to explain the characteristic temperature spikes observed when the lasers are detuned to either side of the Raman resonance condition.

3.1 Cooling Lithium in One-Dimension

We begin our analysis of gray molasses cooling systems by simulating systems analogous to lithium in one dimension. This system is ideal for simulation, because it has a relatively narrow transition. In the D_1 line of lithium, $\Gamma \approx 100\omega_r$ [16]. In the experimental paper where gray molasses was first observed in lithium 7 [8], the largest values used were $\Omega_p \approx \Delta_p \approx \Delta_r \approx 4.5\Gamma$, where Δ_p and Δ_r are the detunings of the principal and repumper lasers, respectively. When $\Delta_p = \Delta_r$, the Raman condition, $\delta = \Delta_p - \Delta_r = 0$, is met, and we anticipate the formation of dark states. We will discuss exactly why this condition is required for dark states to form in section 3.2. In order for cooling to occur, there must be a phase introduced between the lasers addressing each manifold. If no phase is introduced between the manifolds, we find that the system quickly ceases to evolve as it enters velocity independent dark states. The nature of these dark states will be also be discussed

in section 3.2.

Lithium consists of three internal energy manifolds, two ground state manifolds separated by a microwave frequency, and an excited manifold. As illustrated in Fig. 3.1, these manifolds are defined by the higher energy ground state $F_g = 2$, and lower energy ground state $F_g = 1$, and an excited state $F_e = 2$. A pair of low power σ_+ - σ_- repumping lasers address the $F_g = 1$ to $F_e = 2$ transition, and a pair of higher powered principle laser address the $F_g = 2$ to $F_e = 2$ transition.

First, in order to disrupt velocity independent dark states, we generate a random phase at every time step and apply it to each repumping laser. This results in the system continuing to evolve. However, we find in Fig. 3.2 that the system does not cool successfully as the variance of the distribution continues to increase. We find that although this configuration does not successfully cool the system, some population appears to be trapped at low velocities, indicated by the spikes in the momentum distribution at the center of the distribution, with peaks separated by one $\hbar k$. One possible explanation for the failure to cool under this configuration is that we can only alter the random phase once per time step. In a real system, this alteration could be made arbitrarily frequent throughout the experiment. If this result is physical, it indicates that the system's cooling is strongly related to the velocity dependent dark states, which are disrupted by the random phase. We will discuss these states in more detail in sections 2.2.1 and 3.2.

Next, we analyze a system wherein rather than a random phase, we introduce a detuning δ on each repumping laser. So, Eq. (2.7) is modified to read

$$\begin{aligned}\tilde{\hat{H}} = &\sum_{l=x,y,z} \hbar\Delta_1|g_1\rangle\langle g_1| + \hbar\Delta_2|g_2\rangle\langle g_2| \\ &+ \sum_{l=x,y,z} \frac{\hbar\Omega_{1,l}}{2}\left(e^{-i\delta t}\hat{\sigma}_1^- e^{-i\omega_r t(2\beta+1)}|\beta\rangle\langle\beta+1| + h.c.\right) + \frac{\hbar\Omega_{1,l}}{2}\left(e^{i\delta t}\hat{\sigma}_1^- e^{i\omega_r t(2\beta-1)}|\beta\rangle\langle\beta-1| + h.c.\right) \\ &+ \sum_{l=x,y,z} \frac{\hbar\Omega_{2,l}}{2}\left(\hat{\sigma}_2^- e^{-i\omega_r t(2\beta+1)}|\beta\rangle\langle\beta+1| + h.c.\right) + \frac{\hbar\Omega_{2,l}}{2}\left(\hat{\sigma}_2^- e^{i\omega_r t(2\beta-1)}|\beta\rangle\langle\beta-1| + h.c.\right).\end{aligned} \tag{3.1}$$

The time dependent phase may be considered a detuning term, loaded onto the field, rather than rotated out in the interaction picture. In this system, we observe significant time dependent

effects demonstrated in Fig. 3.3. Furthermore, we find the system reached temperatures well below the Doppler limit, at $T^{'} = 10.8$ nearing the recoil limit itself. There appears to be Rabi oscillations between the two manifolds, with each cycle driving the temperature lower. Furthermore, there are notable spikes in the population at momentum states separated by $\hbar k$, indicating the presence of relatively stable dark states. We will provide further analysis for the time dependence of this system in section 3.2.

Figure 3.1: This figure denotes the level structure of lithium 7. There are five excited states in a single manifold $F_e = 2$, separated from eight ground states in two manifolds, $F_g = 1$ and $F_g = 2$. These two manifolds are separated by a microwave transition, and there is no spontaneous emission, or atom field interaction driving transitions between them. Each ground manifold is connected to the excited state by a separate pair of σ_+ - σ_- lasers.

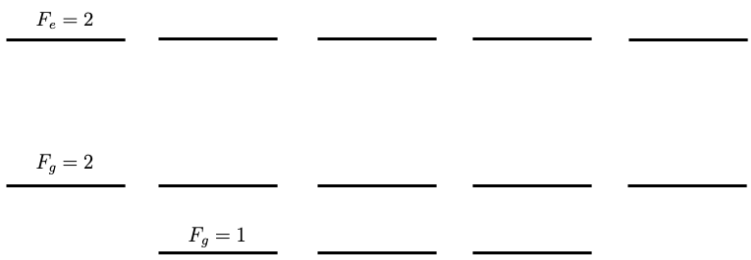

3.2 Six-Level Lithium System

In this section we extend Reiter and Sørenson operator formalism to address the lithium system. We provide some basic analysis of the dark states of the system, compare these derivations to our Monte Carlo wave function results, and create a platform for future analysis using this method. Unlike the previous section, our state kets must now account for manifold degeneracy, so we write the atomic state $|F, m, \beta\rangle$, where F corresponds to the manifold degeneracy, m corresponds to the magnetic quantum number, and β corresponds to the dimensionless momentum.

We begin by defining our ground state Hamiltonian, assuming we have moved into a rotating frame where the lasers addressing each manifold are equally detuned from the excited state:

Figure 3.2: In this plot we have fixed $\Gamma = 100$, the repumping laser $\Omega_r = 134$, the principle laser $\Omega_p = 450$, and $\Delta_r = \Delta_p = 4.5\Gamma$. The top plot is the momentum distribution, averaged over 800 trajectories, between times $\frac{2000}{\Gamma}$ and $\frac{2200}{\Gamma}$. The red line is a Gaussian fit of this distribution, with a temperature corresponding to $T' = 68.0$. The bottom plot is the dimensionless temperature value with respect to time, extracted from the variance at each time step.

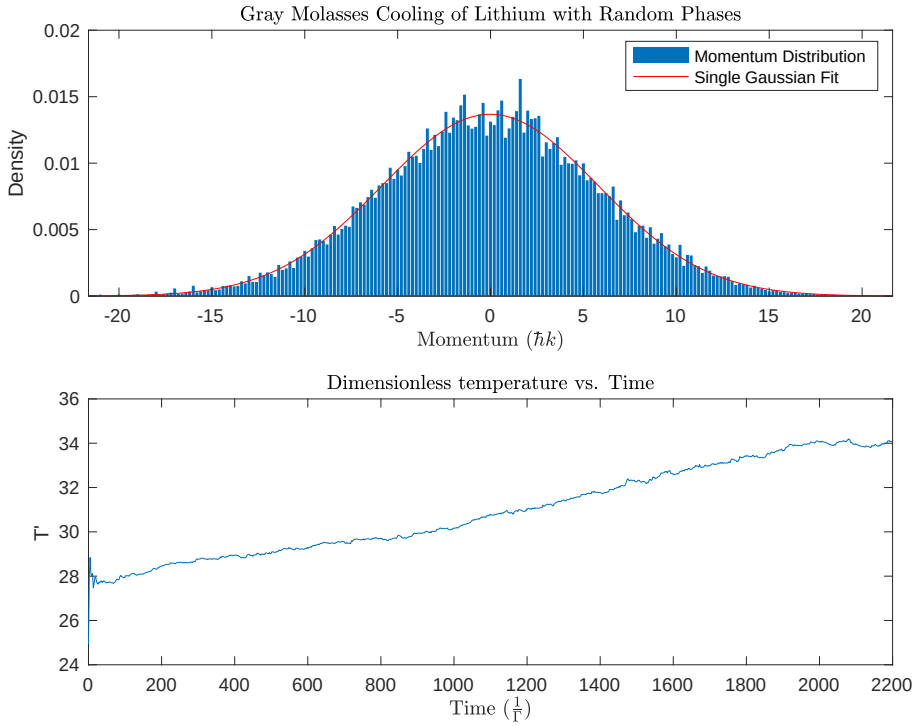

Figure 3.3: In these plots we have fixed $\Gamma = 100$, the repumping laser $\Omega_r = 134$, the principal laser $\Omega_p = 450$, and $\Delta_r = \Delta_p = 4.5\Gamma$. We have introduced a $\delta = 2$ detuning between the lasers. The top left plot is the dimensionless temperature over time, extracted from the variance of the distribution. The top right is the population in each manifold over time. The bottom plot is the momentum distribution, averaged over 800 trajectories, between times $\frac{2000}{\Gamma}$ and $\frac{2200}{\Gamma}$. The red line is a Gaussian fit of this distribution, with a temperature corresponding to $T^{'} = 10.8$.

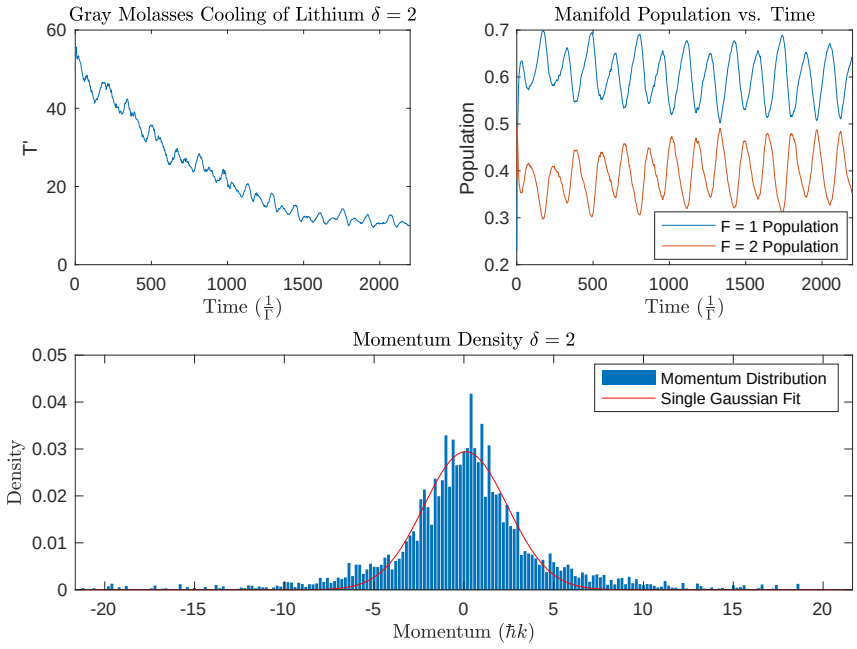

$$\hat{H}_g = -\Delta \sum_{l=-1}^{1} |F=1, m=l, \beta\rangle\langle F=1, m=l, \beta| - \Delta \sum_{l=-2}^{2} |F=2, m=l, \beta\rangle\langle F=2, m=l, \beta| \ . \tag{3.2}$$

With the ground state defined, we note that there are 21 possible transitions connecting the various ground states to the excited states. For the interaction Hamiltonian, we are only concerned with σ_+ and σ_- transitions, so it takes takes the form:

$$\begin{aligned}
\hat{V} = &\sum_{l=-2}^{1} c_l \frac{\Omega_2}{2} \big(e^{-it(2\beta+1)} |F=2, m=l, \beta\rangle\langle \beta+1, m=l+1, e| \\
&\qquad + e^{it(2\beta+1)} |e, m=l+1, \beta+1\rangle\langle \beta, m=l, F=2| \big) \\
&+ \sum_{l=-1}^{2} c_l \frac{\Omega_2}{2} \big(e^{it(2\beta-1)} |F=2, m=l, \beta\rangle\langle \beta-1, m=l-1, e| \\
&\qquad + e^{-it(2\beta+1)} |e, m=l-1, \beta-1\rangle\langle \beta, m=l, F=2| \big) \\
&+ \sum_{l=-1}^{0} c_l \frac{\Omega_1}{2} \big(e^{i\delta t} e^{-it(2\beta+1)} |F=1, m=l, \beta\rangle\langle \beta+1, m=l+1, e| \\
&\qquad + e^{-i\delta t} e^{it(2\beta+1)} |e, m=l+1, \beta+1\rangle\langle \beta, m=l, F=1| \big) \\
&+ \sum_{l=0}^{1} c_l \frac{\Omega_1}{2} \big(e^{-i\delta t} e^{it(2\beta-1)} |F=1, m=l, \beta\rangle\langle \beta-1, m=l-1, e| \\
&\qquad + e^{i\delta t} e^{-it(2\beta+1)} |e, m=l-1, \beta-1\rangle\langle \beta, m=l, F=1| \big) \ .
\end{aligned} \tag{3.3}$$

The c_l terms are the Clebsch-Gordon coefficients of each transition. Because the raising and lowering operators result in an increase and decrease in the magnetic quantum number, effective transitions between ground states occur only between magnetic quantum numbers separated by two, or of the form $|m = l \pm 1\rangle\langle m = l \mp 1|$. This means that even magnetic states are connected to evens, and odds to odds. These two families of quantum states are connected to one another via spontaneous emission. For the sake of simplicity and brevity, we will address only the even family of states. This means that after the adiabatic elimination of the excited states, we will be concerned only with the population of four ground states, $|F=2, m=-2, \beta\rangle$, $|F=2, m=0, \beta\rangle$, $|F=2, m=2, \beta\rangle$, $|F=1, m=0, \beta\rangle$, and the transitions between these states. We find that, after each transition is

accounted for, the effective Hamiltonian takes the form

$$\begin{aligned}
\hat{H}_{eff} = \hat{H}_g &- \frac{1}{3}\frac{\Omega_2^2}{4\Delta}|F=2,m=-2,\beta\rangle\langle\beta,m=-2,F=2| \\
&- \frac{\Omega_2^2}{4\Delta}|F=2,m=0,\beta\rangle\langle\beta,m=0,F=2| \\
&- e^{it4\beta}\frac{1}{\sqrt{6}}\frac{\Omega_2^2}{4\Delta}|F=2,m=0,\beta+1\rangle\langle\beta-1,m=-2,F=2| \\
&- e^{-it4\beta}\frac{1}{\sqrt{6}}\frac{\Omega_2^2}{4\Delta}|F=2,m=-2,\beta-1\rangle\langle\beta+1,m=0,F=2| \\
&- \frac{1}{3}\frac{\Omega_2^2}{4\Delta}|F=2,m=2,\beta\rangle\langle\beta,m=2,F=2| \\
&- e^{-it4\beta}\frac{1}{\sqrt{6}}\frac{\Omega_2^2}{4\Delta}|F=2,m=0,\beta-1\rangle\langle\beta+1,m=2,F=2| \\
&- e^{it4\beta}\frac{1}{\sqrt{6}}\frac{\Omega_2^2}{4\Delta}|F=2,m=2,\beta+1\rangle\langle\beta-1,m=0,F=2| \\
&- \frac{\Omega_1^2}{4\Delta}|F=1,m=0,\beta\rangle\langle\beta,m=0,F=1| \\
&- \frac{\Omega_1\Omega_2}{8\Delta}(e^{i\delta t}+e^{-i\delta t})|F=1,m=0,\beta\rangle\langle\beta,m=0,F=2| \\
&- \frac{\Omega_1\Omega_2}{8\Delta}(e^{i\delta t}+e^{-i\delta t})|F=2,m=0,\beta\rangle\langle\beta,m=0,F=1| \\
&- e^{it4\beta}e^{i\delta t}\frac{1}{\sqrt{6}}\frac{\Omega_1\Omega_2}{4\Delta}|F=1,m=0,\beta+1\rangle\langle\beta-1,m=-2,F=2| \\
&- e^{-it4\beta}e^{-i\delta t}\frac{1}{\sqrt{6}}\frac{\Omega_1\Omega_2}{4\Delta}|F=2,m=-2,\beta-1\rangle\langle\beta+1,m=0,F=1| \\
&- e^{-it4\beta}e^{-i\delta t}\frac{1}{\sqrt{6}}\frac{\Omega_1\Omega_2}{4\Delta}|F=1,m=0,\beta-1\rangle\langle\beta+1,m=2,F=2| \\
&- e^{it4\beta}e^{i\delta t}\frac{1}{\sqrt{6}}\frac{\Omega_1\Omega_2}{4\Delta}|F=2,m=2,\beta+1\rangle\langle\beta-1,m=0,F=1| \ .
\end{aligned} \tag{3.4}$$

A more rigorous derivation for this effective Hamiltonian can be found in appendix B. In the above Hamiltonian, it must be noted that β corresponds to the intermediate momentum value of the given transition, and may be different for various transitions. For example, if at $m = 0$, we had $\beta = 0$, the β value for the $m = 0$ to $m = \pm 2$ transitions would be $\beta = \pm 1$.

We can now construct a system of four coupled equations, describing to the population in each of the four even ground states, a_{FM}, where F indicates the manifold and M indicates magnetic number. First, we note the constraint $(a_{10})^2 + (a_{20})^2 + (a_{2-2})^2 + (a_{22})^2 = 1$, which indicates that our population is normalized. We further specify that we are only concerned with the family of

momentum states centered around a given momentum k, at the m = 0 state. Thus, the m = 2 state would have momentum $k+2$, and m = - 2 has momentum $k-2$. Our equations now become,

$$-a_{20}\frac{\Omega_2^2}{4\Delta} = a_{10}\frac{\Omega_1\Omega_2}{4\Delta}\cos\delta t + a_{2-2}\frac{\Omega_2^2}{4\sqrt{6}\Delta}e^{4itk} + a_{22}\frac{\Omega_2^2}{4\sqrt{6}\Delta}e^{-4itk}\ , \tag{3.5}$$

$$-a_{10}\frac{\Omega_1^2}{4\Delta} = a_{20}\frac{\Omega_1\Omega_2}{4\Delta}\cos\delta t + a_{2-2}\frac{\Omega_1\Omega_2}{4\sqrt{6}\Delta}e^{i\theta t}e^{4itk} + a_{22}\frac{\Omega_1\Omega_2}{4\sqrt{6}\Delta}e^{-i\theta t}e^{-4itk}\ , \tag{3.6}$$

$$-a_{2-2}\frac{1}{3}\frac{\Omega_2^2}{4\Delta} = a_{20}\frac{\Omega_2^2}{4\sqrt{6}\Delta}e^{-4itk} + a_{10}\frac{\Omega_1\Omega_2}{4\sqrt{6}\Delta}e^{-i\delta t}e^{-4itk}\ , \tag{3.7}$$

$$-a_{22}\frac{1}{3}\frac{\Omega_2^2}{4\Delta} = a_{20}\frac{\Omega_2^2}{4\sqrt{6}\Delta}e^{4itk} + a_{10}\frac{\Omega_1\Omega_2}{4\sqrt{6}\Delta}e^{i\delta t}e^{4itk}\ . \tag{3.8}$$

Due to the symmetry in this system, if we allow $a_{2-2} = a_{22} = b$, our equations become

$$-a_{20}\frac{\Omega_2^2}{4\Delta} = a_{10}\frac{\Omega_1\Omega_2}{4\Delta}\cos\delta t + b\frac{\Omega_2^2}{8\sqrt{6}\Delta}\cos 4kt\ , \tag{3.9}$$

$$-a_{10}\frac{\Omega_1^2}{4\Delta} = a_{20}\frac{\Omega_1\Omega_2}{4\Delta}\cos\delta t + b\frac{\Omega_1\Omega_2}{4\sqrt{6}\Delta}\cos(\delta+4k)t\ , \tag{3.10}$$

$$-b\frac{1}{3}\frac{\Omega_2^2}{4\Delta} = a_{20}\frac{\Omega_2^2}{4\sqrt{6}\Delta}e^{-4itk} + a_{10}\frac{\Omega_1\Omega_2}{4\sqrt{6}\Delta}e^{-i\delta t}e^{-4itk}\ , \tag{3.11}$$

$$-b\frac{1}{3}\frac{\Omega_2^2}{4\Delta} = a_{20}\frac{\Omega_2^2}{4\sqrt{6}\Delta}e^{4itk} + a_{10}\frac{\Omega_1\Omega_2}{4\sqrt{6}\Delta}e^{i\delta t}e^{4itk}\ . \tag{3.12}$$

We begin by studying the case where $b = 0$, and $\delta = 0$. The system easily reduces into a dark state where $a_{10} = -a_{20}\frac{\Omega_2}{\Omega_1}$. This dark state is completely velocity independent. Because of these velocity independent dark state, the system ceases to evolve and fails to cool the atoms. The introduction of a $\delta \neq 0$ disrupts the dark state by introducing a time-dependence to these equations, resulting and population transfer, and consequentially spontaneous emission.

Similarly to the previous section, the introduction of the δ term results in velocity dependent dark states. By letting $\delta = -4k$, $a_{20} = 0$, and keeping the assumption that $a_{2-2} = a_{22} = b$, we find

$$-a_{10}\frac{\Omega_1\Omega_2}{4\Delta} = b\frac{\Omega_2^2}{2\sqrt{6}\Delta}\ , \tag{3.13}$$

$$-a_{10}\frac{\Omega_1^2}{4\Delta} = b\frac{\Omega_1\Omega_2}{2\sqrt{6}\Delta}\ , \tag{3.14}$$

$$-b\frac{1}{3}\frac{\Omega_2^2}{4\Delta} = a_{10}\frac{\Omega_1\Omega_2}{4\sqrt{6}\Delta} \ , \tag{3.15}$$

$$-b\frac{1}{3}\frac{\Omega_2^2}{4\Delta} = a_{10}\frac{\Omega_1\Omega_2}{4\sqrt{6}\Delta} \ . \tag{3.16}$$

The solution to this system of equation $a_{10} = -b\frac{\sqrt{6}\Omega_2}{3\Omega_1}$. Therefore, we have selected a dark state in the system at momentum $k = -\frac{\delta}{4}$. We note that a similar calculation can be done on the odd magnetic numbers, by following the procedure in appendix B.

We have predicted that introducing a detuning between the lasers will shift the resonant momentum of the dark state, which will affect the equilibrium temperature of the system. This represents a possible explanation for the off resonant momentum spikes in gray molasses configuration. In Fig. 3.4, we find that indeed, the temperature tends to increase with δ. We note that calculating this plot for greater detuning values becomes increasing difficult, as it requires smaller time steps, and wider momentum grids as temperature increases. We can qualitatively confirm our findings of velocity selective dark states from the momentum histogram when $\delta = 16$. In Fig. 3.5 it is clear that some of the population has shifted in the negative direction by approximately $4\hbar k$, which agrees with our prediction that the dark state will be centered around $k = -\frac{\delta}{4}$.

3.3 Fano Profiles of the Simplified Model

Another explanation for the off-resonance temperature spikes in gray molasses derives from Fano profiles. These mathematical objects are found by solving the optical Bloch equations (OBEs), for a three level system. Originally solved in [2], the OBEs differ greatly from the fully quantum solution employed in Monte Carlo wave functions, and adiabatically eliminated solution from Reiter and Sørensen, because the OBEs are a semi-classical approximation of the wave function. Although the OBEs are a useful approximation of wave function, particularly in identifying equilibrium temperatures, we will not go into depth on their solutions in this thesis. Following the procedure given by [15, 7], and assuming that the decay rate Γ into both ground states is equivalent, the fano profiles for lithium and YO take the form Fig 3.6.

The width between the spikes in these profiles corresponds almost exactly to the width

Figure 3.4: In this plot we calculate the equilibrium temperature for $\delta = 2, 4, \&16$. Each point is averaged over 800 trajectories from time $\frac{2000}{\Gamma}$ to $\frac{2200}{\Gamma}$. The error bars indicate 95% confidence of the least squares Gaussian fit.

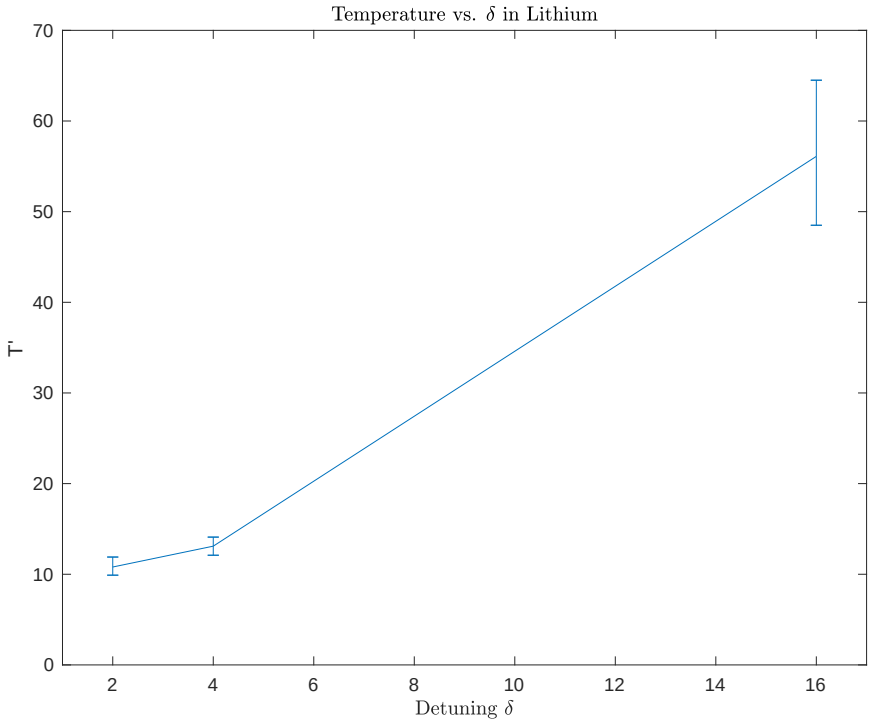

Figure 3.5: In this plot we have fixed $\Gamma = 100$, the repumping laser $\Omega_r = 134$, the principal laser $\Omega_p = 450$, and $\Delta_r = \Delta_p = 4.5\Gamma$. We have introduced a $\delta = 16$ detuning between the lasers. The momentum distribution, averaged over 800 trajectories, between times $\frac{2000}{\Gamma}$ and $\frac{2200}{\Gamma}$. The green line is a Gaussian fit of this distribution, with a temperature corresponding to $T^{'} = 56.1$.

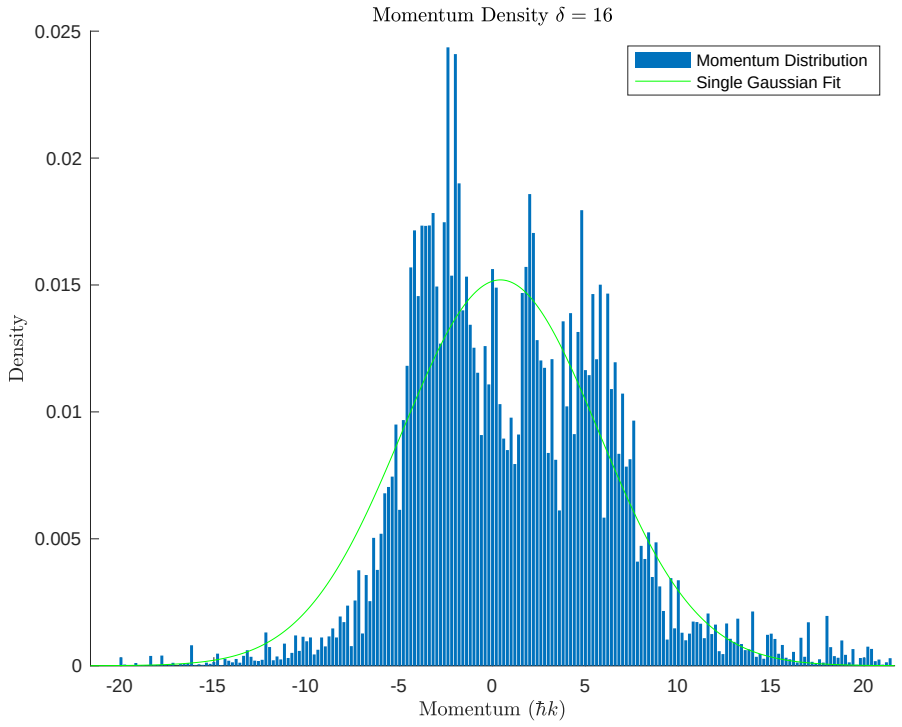

between the spikes in temperatures around resonance found in the Lithium and YO experiments. In general, equilibrium temperatures when calculated from the OBEs are linearly proportional to the excited state population. This indicates that there is there is Fano resonance akin to that found in [19]. Extending the three level qualitative model to the complete YO and lithium systems requires a rigorous solution to the OBEs, and is beyond the scope of this thesis.

Figure 3.6: In this plot we have fixed have assumed that the emission rate into both ground states are equivalent. On the left plot, we have let $\Delta_r = -4.5\Gamma$, $\Omega_r = 1.34\Gamma$, and $\Omega_p = 4.5\Gamma$. On the right plot we have let $\Delta_r = -12.5\Gamma$, $\Omega_r = 0.86\Gamma$, and $\Omega_p = 1.26\Gamma$.

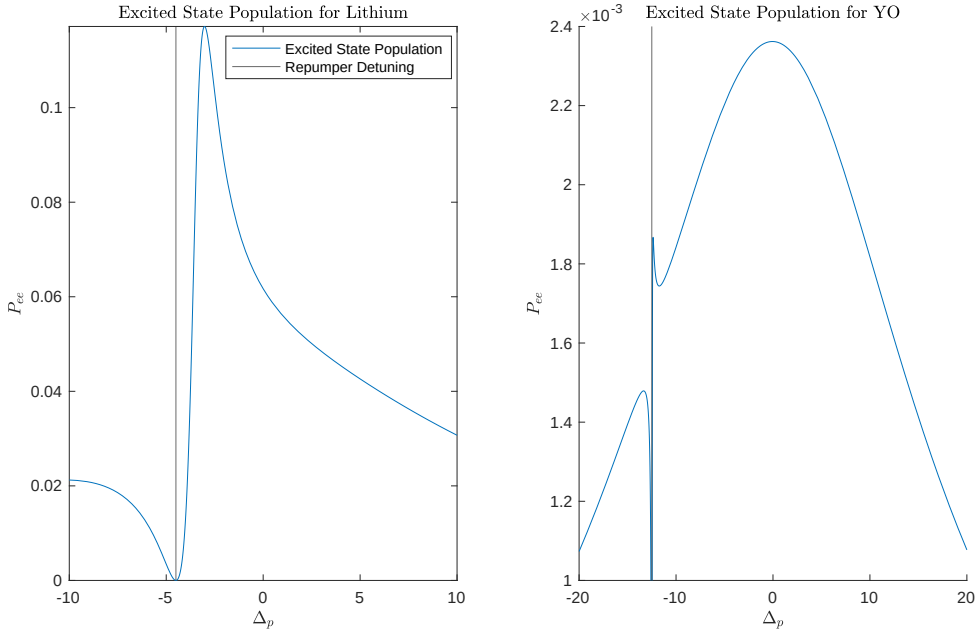

Chapter 4

Summary & Conclusion

In Chapter 1 of this thesis we present motivation for a project to provide a theoretical framework for off-resonant temperature phenomena that occur in Gray Molasses Cooling systems such as lithium, rubidium, and YO. We also review the basics of laser cooling in Doppler, Polarization Gradient, and VSCPT configurations. In chapter 2 we extend the Monte Carlo wave function technique to multiple energy manifolds and dimensions. We demonstrate a simplification in the algorithm, which employs the Hamiltonian's time reversal symmetry to allow for easy modification of the atomic system. We also introduce Reiter and Sørensen adiabatic elimination of the excited state as a technique to analytically study Hamiltonians for systems near resonance. In chapter 3 we apply both the Monte Carlo wave function methodology and the adiabatic elimination technique to a lithium-7 GMC configuration, in order to study the system's behavior near the Raman resonance condition. We also qualitatively compare our results to the Fano profile of simplified three-level systems.

To achieve our goals we derived a widely applicable Hamiltonian for Monte Carlo wave functions, and wrote flexible code capable of simulating arbitrarily many energy manifolds and degenerate states, in one, two and three dimensions. We added momentum dependence to the Reiter and Sørensen operator formalism, and demonstrated a simple technique for constructing large Hamiltonians. Using these techniques, we were able to analytically and numerically describe GMC in lithium. However, more work is required to construct a complete theory of the gray molasses configuration. Due to the narrow transition of YO, which is less than twice the recoil frequency,

and the unique internal structure, we have not yet simulated this configuration. A combination of longer integration times, analytic approximations, and fictional parameters may be required in order to simulate the YO configuration. A formal description of the equilibrium temperatures for gray molasses is still required in order for us fully understand the physical mechanisms at play. Such a description will allow us to predict the ideal parameter regime for maximally cooling these systems. Detuning dependent dark states and Fano profiles show promise for developing a complete theory of gray molasses cooling, and more work is required in this area to convert the qualitative descriptions at equilibrium into rigorous theory. Since the the momentum distributions are non-Gaussian, an alternative approach to defining temperature may be required. Next steps will include analytically linking these momentum distributions to parameters such as detuning and intensity, and deriving an expression for temperature based upon these distributions.

Bibliography

[1] Limit of doppler cooling. J. Opt. Soc. Am. B, 6(11):2046–2057, Nov 1989.

[2] F. Arecchi and R. Bonifacio. Theory of optical maser amplifiers. IEEE Journal of Quantum Electronics, 1(4):169–178, 1965.

[3] A. Aspect, E. Arimondo, R. Kaiser, N. Vansteenkiste, and C. Cohen-Tannoudji. Laser cooling below the one-photon recoil energy by velocity-selective coherent population trapping. Phys. Rev. Lett., 61:826–829, Aug 1988.

[4] J. Dalibard and C. Cohen-Tannoudji. Laser cooling below the doppler limit by polarization gradients: simple theoretical models. J. Opt. Soc. Am. B, 6(11):2023–2045, Nov 1989.

[5] Shiqian Ding, Yewei Wu, Ian A. Finneran, Justin J. Burau, and Jun Ye. Sub-doppler cooling and compressed trapping of yo molecules at μK temperatures. Phys. Rev. X, 10:021049, Jun 2020.

[6] M Drewsen, U Drodofsky, C Weber, G Schreiber, and J Mlynek. Sisyphus polarization gradient laser cooling of cr atoms on theJ= 3, , 3 and 4 transitions. Journal of Physics B: Atomic, Molecular and Optical Physics, 29(23):L843–L850, dec 1996.

[7] U. Fano. Effects of configuration interaction on intensities and phase shifts. Phys. Rev., 124:1866–1878, Dec 1961.

[8] Andrew T. Grier, Igor Ferrier-Barbut, Benno S. Rem, Marion Delehaye, Lev Khaykovich, Frédéric Chevy, and Christophe Salomon. Λ-enhanced sub-doppler cooling of lithium atoms in D_1 gray molasses. Phys. Rev. A, 87:063411, Jun 2013.

[9] T.W. Hänsch and A.L. Schawlow. Cooling of gases by laser radiation. Optics Communications, 13(1):68–69, 1975.

[10] M. Holland, S. Marksteiner, P. Marte, and P. Zoller. Measurement induced localization from spontaneous decay. Phys. Rev. Lett., 76:3683–3686, May 1996.

[11] J Javanainen. Polarization gradient cooling in three dimensions: comparison of theory and experiment. 27(3):L41–L47, feb 1994.

[12] Zhong-Hua Ji, Jin-Peng Yuan, Yan-Ting Zhao, Xue-Fang Chang, Lian-Tuan Xiao, and Suo-Tang Jia. Systematically investigating the polarization gradient cooling in an optical molasses of ultracold cesium atoms. Chinese Physics B, 23(11):113702, nov 2014.

[13] J. Lawall, F. Bardou, B. Saubamea, K. Shimizu, M. Leduc, A. Aspect, and C. Cohen-Tannoudji. Two-dimensional subrecoil laser cooling. Phys. Rev. Lett., 73:1915–1918, Oct 1994.

[14] Paul D. Lett, Richard N. Watts, Christoph I. Westbrook, William D. Phillips, Phillip L. Gould, and Harold J. Metcalf. Observation of atoms laser cooled below the doppler limit. Phys. Rev. Lett., 61:169–172, Jul 1988.

[15] B. Lounis and C. Cohen-Tannoudji. Coherent population trapping and fano profiles. Journal De Physique II, 2:579–592, 1992.

[16] Harold J. Metcalf and Peter Van der Straten. Laser cooling and trapping. Graduate Texts in Contemporary Physics, 1999.

[17] Klaus Mølmer, Yvan Castin, and Jean Dalibard. Monte carlo wave-function method in quantum optics. J. Opt. Soc. Am. B, 10(3):524–538, Mar 1993.

[18] M.A. Ol'shaniî and V.G. Minogin. Three-dimensional velocity-selective coherent population trapping of a (3+3)-level atom. Optics Communications, 89(5):393–398, 1992.

[19] Mu Qiao, Ye Wang, Zhengyang Cai, Botao Du, Pengfei Wang, Chunyang Luan, Wentao Chen, Heung-Ryoul Noh, and Kihwan Kim. Double-electromagnetically-induced-transparency ground-state cooling of stationary two-dimensional ion crystals. Phys. Rev. Lett., 126:023604, Jan 2021.

[20] Jarrod T Reilly. Entropy Removal and Coherence with Lasers. Bachelor's thesis, University of Colorado Boulder, Nov 2020.

[21] Florentin Reiter and Anders S. Sørensen. Effective operator formalism for open quantum systems. Phys. Rev. A, 85:032111, Mar 2012.

[22] Sara Rosi, Alessia Burchianti, Stefano Conclave, Devang S. Naik, Giacomo Roati, Chiara Fort, and Francesco Minardi. -enhanced grey molasses on the d2 transition of rubidium-87 atoms. 8(1):1301.

[23] J. J. Sakurai and Jim Napolitano. Modern Quantum Mechanics. Cambridge University Press, 2021.

[24] G. Salomon, L. Fouché, P. Wang, A. Aspect, P. Bouyer, and T. Bourdel. Gray-molasses cooling of 39 k to a high phase-space density. EPL (Europhysics Letters), 104:63002, 2013.

[25] Daniel A. Steck. Quantum and Atom Optics. University of Oregon, 2021.

[26] D. J. Wineland, R. E. Drullinger, and F. L. Walls. Radiation-pressure cooling of bound resonant absorbers. Phys. Rev. Lett., 40:1639–1642, Jun 1978.

Appendix A

The Interaction Picture for a Two-Level Atom

We begin with the simplest laser cooling model, Doppler cooling. In this configuration, a two-level atom with an electronic ground state $|g\rangle$ and excited state $|e\rangle$ separated by frequency ω_a, interacts with 6 red-detuned classical fields, one from each positive and negative spatial direction. We represent the particles external degrees of freedom in a discrete momentum space, spaced by units of $\hbar k$, in each spatial direction: $|p_x\rangle$, $|p_y\rangle$, and $|p_z\rangle$. Thus, in the lab frame, the Hamiltonian is given by

$$\hat{H}_{\text{org}} = \frac{\hbar\omega_a}{2}\hat{\sigma}_z \otimes \hat{\mathbb{I}}_p + \sum_{l=x,y,z}\left(\hat{\mathbb{I}}_a \otimes \hat{\mathbb{I}}_p\right)\frac{\hat{p}_l^2}{2m} + \hat{H}_{\text{int},l}, \tag{A.1}$$

where we have defined the atomic Pauli z operator as $\hat{\sigma}_z = |e\rangle\langle e| - |g\rangle\langle g|$, the momentum operator in direction l as $\hat{p}_l = \sum_{p_l} p_l |p_l\rangle\langle p_l|$, and the identity operator of the internal and external subspaces as $\hat{\mathbb{I}}_a = |g\rangle\langle g| + |e\rangle\langle e|$ and $\hat{\mathbb{I}}_p = \bigotimes_{l=x,y,z}\sum_{p_l}|p_l\rangle\langle p_l|$. The interaction Hamiltonian in spatial direction l after the dipole and rotating-wave approximations is given by

$$\hat{H}_{\text{int},l} = \frac{\hbar\Omega_l}{2}\left(\hat{\sigma}_- e^{-i[k\hat{x}_l - \omega_l t]} + h.c.\right) + \frac{\hbar\Omega_l}{2}\left(\hat{\sigma}_- e^{i[k\hat{x}_l + \omega_l t]} + h.c.\right), \tag{A.2}$$

where we have assumed that the right and left lasers in spatial direction l have the same frequency ω_l that is time-independent. Here, $\hat{x}_l$ is the position operator for spatial direction l, the internal Pauli lowering (raising) operator is defined as $\hat{\sigma}_- = |g\rangle\langle e|$ ($\hat{\sigma}_+|e\rangle\langle g|$), the momentum shift operator can be written as $\exp[ik\hat{x}_l] = \sum_{p_l}|p_l + \hbar k\rangle\langle p_l|$, and the Rabi frequency is given by [25]

$$\Omega_l = -\frac{E_{0,l}}{\hbar}\langle g|\hat{\varepsilon}_l \cdot \hat{\boldsymbol{d}}|e\rangle, \tag{A.3}$$

where $E_{0,l}$ is the magnitude of the electric field, $\hat{\varepsilon}_l$ is the unit polarization vector of the field, and

$$\hat{\boldsymbol{d}} = -e\hat{\boldsymbol{r}} = \langle g|\hat{\boldsymbol{d}}|e\rangle \left(|g\rangle\langle e| + |e\rangle\langle g|\right), \tag{A.4}$$

is the dipole operator with electron position $\hat{\boldsymbol{r}}$.

Dropping the identity operators from our calculation, we now move into an interaction picture defined by

$$\hat{H}' = \frac{\hbar\omega}{2}\hat{\sigma}_z + \sum_{l=x,y,z} \frac{\hat{p_l}^2}{2m}, \tag{A.5}$$

where we have assumed each laser has the same frequency ω and defined $\omega_r = \hbar k^2/(2m)$ as the recoil frequency. We thus obtain [20]

$$\hat{H} = -\frac{\hbar\Delta}{2}\hat{\sigma}_z + \sum_{l=x,y,z} \frac{\hbar\Omega_l}{2}\left(\hat{\sigma}_- e^{-ik\left[\hat{x}_l + \frac{\hat{p}_l t}{m}\right]} + h.c.\right) + \frac{\hbar\Omega_l}{2}\left(\hat{\sigma}_- e^{ik\left[\hat{x}_l + \frac{\hat{p}_l t}{m}\right]} + h.c.\right), \tag{A.6}$$

where $\Delta = \omega - \omega_a$ is the detuning of every laser in the lab frame. Using the Baker-Campbell-Hausdorff lemma, specifically the Zassenhaus formula

$$e^{t\left(\hat{A}+\hat{B}\right)} = e^{t\hat{A}} e^{t\hat{B}} e^{-\frac{t^2}{2}\left[\hat{A},\hat{B}\right]} e^{\frac{t^3}{6}\left(2\left[\hat{B},\left[\hat{A},\hat{B}\right]\right]+\left[\hat{A},\left[\hat{A},\hat{B}\right]\right]\right)} \ldots \tag{A.7}$$

where $\left[\hat{A},\hat{B}\right] = \hat{A}\hat{B} - \hat{B}\hat{A}$ is the commutator, we can separate the exponentials to obtain

$$\hat{H} = -\frac{\hbar\Delta}{2}\hat{\sigma}_z + \sum_{l=x,y,z} \frac{\hbar\Omega_l}{2}\left(\hat{\sigma}_- e^{i\omega_r t} e^{-ik\hat{x}_l} e^{-i\frac{k\hat{p}_l t}{m}} + h.c.\right) + \frac{\hbar\Omega_l}{2}\left(\hat{\sigma}_- e^{i\omega_r t} e^{ik\hat{x}_l} e^{i\frac{k\hat{p}_l t}{m}} + h.c.\right). \tag{A.8}$$

We now define $\hat{\beta}_l = \hat{p}_l/(\hbar k) = \sum_{\beta_l} \beta_l |\beta_l\rangle\langle\beta_l|$ with momentum number $\beta_l = p_l/(\hbar k)$ and eigenstates $|\beta_l\rangle = |p_l/(\hbar k)\rangle$ such that

$$\hat{H} = -\frac{\hbar\Delta}{2}\hat{\sigma}_z + \sum_{l=x,y,z} \frac{\hbar\Omega_l}{2}\left(\hat{\sigma}_- e^{-ik\hat{x}_l} e^{-2i\omega_r\hat{\beta}_l t} e^{i\omega_r t} + h.c.\right) + \frac{\hbar\Omega_l}{2}\left(\hat{\sigma}_- e^{ik\hat{x}_l} e^{2i\omega_r\hat{\beta}_l t} e^{i\omega_r t} + h.c.\right) \tag{A.9}$$

Since the momentum shift operators is now given by $\exp\left[ik\hat{x}_l\right] = \sum_{\beta_l} |\beta_l\rangle\langle\beta_l - 1|$ and $\exp\left[-ik\hat{x}_l\right] = \sum_{\beta_l} |\beta_l\rangle\langle\beta_l + 1|$, we can write

$$\begin{aligned}\hat{H} = &-\frac{\hbar\Delta}{2}\hat{\sigma}_z + \sum_{l=x,y,z} \frac{\hbar\Omega_l}{2}\left(\hat{\sigma}_- \sum_{\beta_l} |\beta_l\rangle\langle\beta_l + 1| e^{-i\omega_r(2\beta_l+1)t} + h.c.\right) \\ &+\frac{\hbar\Omega_l}{2}\left(\hat{\sigma}_- \sum_{\beta_l} |\beta_l\rangle\langle\beta_l - 1| e^{i\omega_r(2\beta_l-1)t} + h.c.\right).\end{aligned} \tag{A.10}$$

From this Hamiltonian, we can calculate the momentum coefficients needed to evolve our code at each time step, by operating on a state vector $|\psi\rangle$

$$|\psi\rangle = \sum_{s=g,e} \sum_{\beta_x} \sum_{\beta_y} \sum_{\beta_z} c_{s\beta_x\beta_y\beta_z} |s\rangle \otimes |\beta_x\rangle \otimes |\beta_y\rangle \otimes |\beta_z\rangle, \tag{A.11}$$

It is trivial to extend our simulation to account for more than two internal energy levels, allowing us to solve more complex internal structures in three dimensions.

Appendix B

Adiabatic elimination of lithium excited states

In this appendix we go through the full derivation for the four level Hamiltonian in 3.2. The employed here can easily be extended to other systems. We begin with the ground state Hamiltonian

$$\hat{H}_g = -\Delta \sum_{l=-1}^{1} |F=1, m=l, \beta\rangle\langle F=1, m=l, \beta| - \Delta \sum_{l=-2}^{2} |F=2, m=l, \beta\rangle\langle F=2, m=l, \beta| \quad \text{(B.1)}$$

and the the interaction Hamiltonian

$$\begin{aligned}
\hat{V} = &\sum_{l=-2}^{1} c_l \frac{\Omega_2}{2} \big(e^{-it(2\beta+1)} |F=2, m=l, \beta\rangle\langle \beta+1, m=l+1, e| \\
&\qquad + e^{it(2\beta+1)} |e, m=l+1, \beta+1\rangle\langle \beta, m=l, F=2| \big) \\
&+ \sum_{l=-1}^{2} c_l \frac{\Omega_2}{2} \big(e^{it(2\beta-1)} |F=2, m=l, \beta\rangle\langle \beta-1, m=l-1, e| \\
&\qquad + e^{-it(2\beta+1)} |e, m=l-1, \beta-1\rangle\langle \beta, m=l, F=2| \big) \\
&+ \sum_{l=-1}^{0} c_l \frac{\Omega_1}{2} \big(e^{i\delta t} e^{-it(2\beta+1)} |F=1, m=l, \beta\rangle\langle \beta+1, m=l+1, e| \\
&\qquad + e^{-i\delta t} e^{it(2\beta+1)} |e, m=l+1, \beta+1\rangle\langle \beta, m=l, F=1| \big) \\
&+ \sum_{l=0}^{1} c_l \frac{\Omega_1}{2} \big(e^{-i\delta t} e^{it(2\beta-1)} |F=1, m=l, \beta\rangle\langle \beta-1, m=l-1, e| \\
&\qquad + e^{i\delta t} e^{-it(2\beta+1)} |e, m=l-1, \beta-1\rangle\langle \beta, m=l, F=1| \big) \ .
\end{aligned} \quad \text{(B.2)}$$

As we do in section 3.2, we focus entirely on the family of even magnetic states. We define the effective Hamiltonian as

$$\hat{H}_{eff}^{even} = -\frac{1}{2}\big[\hat{V}_- \sum_{l=even} (\hat{H}_{nh}^{(l)})^{-1}\hat{V}_+^{(l)} + H.c.\big] + \hat{H}_g \tag{B.3}$$

where the non Hermitian terms are $\hat{H}_{nh}^{(l)} = (\Delta_l - \delta - \frac{i\gamma}{2})|e\rangle\langle e|$. Assuming $|\Delta_l| \gg |\delta|$, then $\hat{H}_{nh}^{(l)} \approx (\Delta_l - \frac{i\gamma}{2})|e\rangle\langle e|$. This calculation is incredibly tedious to conduct term by term, and it is easy to lose track of terms. We present a method wherein the Hamiltonian can be solved in terms of more manageable blocks. Consider a Hamiltonian where three ground $|1\rangle$, $|2\rangle$, and $|3\rangle$, states are coupled to an excited state.

$$\sum_{l=1}^{3}(\hat{H}_{nh}^{(l)})^{-1}\hat{V}_+^{(l)} = c_{1^+}|e\rangle\langle 1| + c_{2^+}|e\rangle\langle 2| + c_{3^+}|e\rangle\langle 3| \tag{B.4}$$

Where c_{l^+} indicates the transition rate from each ground to the excited state, and c_{l^-} the transition rate from the excited to ground state. Applying the lowering operator to this system gives

$$\hat{V}_- \sum_{l=1}^{3}(\hat{H}_{nh}^{(l)})^{-1}\hat{V}_+^{(l)} = (c_{1^-}|1\rangle\langle e| + c_{2^-}|2\rangle\langle e| + c_{3^-}|3\rangle\langle e|)\left(c_{1^+}|e\rangle\langle 1^+| + c_{2^+}|e\rangle\langle 2| + c_{3^+}|e\rangle\langle 3|\right) \tag{B.5}$$

which is equivalent to

$$\hat{V}_- \sum_{l=1}^{3}(\hat{H}_{nh}^{(l)})^{-1}\hat{V}_+^{(l)} = \sum_{l=1}^{3}\sum_{k=1}^{3} c_{l^-}c_{k^+}|l\rangle\langle k| \tag{B.6}$$

What this shows is that each raising and lowering operator is commutative under addition. We can group them however we want, so long as each transition is ultimately accounted for. We therefore elect to separate the Hamiltonian into four portions. $\hat{H}_1$ includes the transitions between $|F = 2, m = 0\rangle$ and $|F = 2, m = -2\rangle$. $\hat{H}_2$ includes the transitions connecting $|F = 1, m = 0\rangle$ to $|F = 2, m = 0\rangle$ and $|F = 2, m = -2\rangle$. $\hat{H}_3$ is the mirror image of $\hat{H}_1$, and includes the transitions from $|F = 2, m = 0\rangle$ and $|F = 2, m = 2\rangle$. Finally $\hat{H}_4$ is the mirror of $\hat{H}_2$ and includes the transitions connecting $|F = 1, m = 0\rangle$ to $|F = 2, m = 0\rangle$ and $|F = 2, m = 2\rangle$. Note that the $|F = 1, m = 0\rangle$ to $|F = 2, m = 0\rangle$ transitions are double counted. This is by design, as the $\hat{H}_2$ transitions pass through the $|E, m = -1\rangle$ state, while the $\hat{H}_4$ transitions pass through the $|E, m = 1\rangle$ state. We now define

$$\hat{H}_{eff}^{even} = \hat{H}_g + \hat{H}_1 + \hat{H}_2 + \hat{H}_3 + \hat{H}_4 \tag{B.7}$$

$\hat{H}_1$ takes the form a similar form as the three level Hamiltonian, because we are only considering two ground states and one excited state

$$\begin{aligned}\hat{H}_1 = &-\frac{1}{3}\frac{\Omega_2^2}{4\Delta_2}|F=2,m=-2,\beta\rangle\langle\beta,m=-2,F=2| \\ &-\frac{1}{2}\frac{\Omega_2^2}{4\Delta_2}|F=2,m=0,\beta\rangle\langle\beta,m=0,F=2| \\ &-e^{it4\beta}\frac{1}{\sqrt{6}}\frac{\Omega_2^2}{4\Delta_2}|F=2,m=0,\beta+1\rangle\langle\beta-1,m=-2,F=2| \\ &-e^{-it4\beta}\frac{1}{\sqrt{6}}\frac{\Omega_2^2}{4\Delta_2}|F=2,m=-2,\beta-1\rangle\langle\beta+1,m=0,F=2|\ .\end{aligned} \tag{B.8}$$

We now add in $\hat{H}_2$, which includes the third ground state, and its effective transitions to the other two

$$\begin{aligned}\hat{H}_2 = &-\frac{1}{2}\frac{\Omega_1^2}{4\Delta_1}|F=1,m=0,\beta\rangle\langle\beta,m=0,F=1| \\ &-e^{i\delta t}\frac{1}{2}\frac{\Omega_1\Omega_2(\Delta_1+\Delta_2)}{8\Delta_1\Delta_2}|F=1,m=0,\beta\rangle\langle\beta,m=0,F=2| \\ &-e^{-i\delta t}\frac{1}{2}\frac{\Omega_1\Omega_2(\Delta_1+\Delta_2)}{8\Delta_1\Delta_2}|F=2,m=0,\beta\rangle\langle\beta,m=0,F=1| \\ &-e^{i\delta t}e^{it4\beta}\frac{1}{\sqrt{6}}\frac{\Omega_1\Omega_2(\Delta_1+\Delta_2)}{8\Delta_1\Delta_2}|F=1,m=0,\beta+1\rangle\langle\beta-1,m=-2,F=2| \\ &-e^{-i\delta t}e^{-it4\beta}\frac{1}{\sqrt{6}}\frac{\Omega_1\Omega_2(\Delta_1+\Delta_2)}{8\Delta_1\Delta_2}|F=2,m=-2,\beta-1\rangle\langle\beta+1,m=0,F=1|\ .\end{aligned} \tag{B.9}$$

$\hat{H}_3$ is the mirror image of $\hat{H}_1$

$$\begin{aligned}\hat{H}_3 = &-\frac{1}{3}\frac{\Omega_2^2}{4\Delta_2}|F=2,m=2,\beta\rangle\langle\beta,m=2,F=2| \\ &-\frac{1}{2}\frac{\Omega_2^2}{4\Delta_2}|F=2,m=0,\beta\rangle\langle\beta,m=0,F=2| \\ &-e^{-it4\beta}\frac{1}{\sqrt{6}}\frac{\Omega_2^2}{4\Delta_2}|F=2,m=0,\beta-1\rangle\langle\beta+1,m=2,F=2| \\ &-e^{it4\beta}\frac{1}{\sqrt{6}}\frac{\Omega_2^2}{4\Delta_2}|F=2,m=2,\beta+1\rangle\langle\beta-1,m=0,F=2|\ ,\end{aligned} \tag{B.10}$$

and $\hat{H}_4$ is the mirror image of $\hat{H}_2$

$$\begin{aligned}
\hat{H}_4 = &-\frac{1}{2}\frac{\Omega_1^2}{4\Delta_1}|F=1,m=0,\beta\rangle\langle\beta,m=0,F=1| \\
&-e^{-i\delta t}\frac{1}{2}\frac{\Omega_1\Omega_2(\Delta_1+\Delta_2)}{8\Delta_1\Delta_2}|F=1,m=0,\beta\rangle\langle\beta,m=0,F=2| \\
&-e^{i\delta t}\frac{1}{2}\frac{\Omega_1\Omega_2(\Delta_1+\Delta_2)}{8\Delta_1\Delta_2}|F=2,m=0,\beta\rangle\langle\beta,m=0,F=1| \\
&-e^{-i\delta t}e^{-it4\beta}\frac{1}{\sqrt{6}}\frac{\Omega_1\Omega_2(\Delta_1+\Delta_2)}{8\Delta_1\Delta_2}|F=1,m=0,\beta-1\rangle\langle\beta+1,m=2,F=2| \\
&-e^{i\delta t}e^{it4\beta}\frac{1}{\sqrt{6}}\frac{\Omega_1\Omega_2(\Delta_1+\Delta_2)}{8\Delta_1\Delta_2}|F=2,m=2,\beta+1\rangle\langle\beta-1,m=0,F=1| \ .
\end{aligned} \tag{B.11}$$

Summing the constituent parts of the effective Hamiltonian, letting $\gamma = 0$, and $\Delta_1 = \Delta_2 = \Delta$, yields equation (3.4). This same strategy can be employed to solve other Hamiltonians, including that corresponding to the odd magnetic terms in the lithium configurations. Furthermore, if we allow $\gamma \neq 0$ and $\Delta_1 \neq \Delta_2$, this formalism could be used to numerically integrate atomic evolution, with the caveat that the Lindblad operators would change according to the technique outlined in [21].